Crack Monitoring from Motion (CMfM): Crack detection and measurement using cameras with non-fixed positions

Valeria Belloni [a,*], Andreas Sjölander [b], Roberta Ravanelli [a], Mattia Crespi [a,c], Andrea Nascetti [d,e]

[a] *Geodesy and Geomatics Division, Department of Civil, Constructional and Environmental Engineering, Sapienza University of Rome, Rome, Italy*
[b] *Division of Concrete Structures, Department of Civil and Architectural Engineering, KTH Royal Institute of Technology, Stockholm, Sweden*
[c] *Sapienza School for Advanced Studies, Sapienza University of Rome, Rome, Italy*
[d] *Geomatics Unit, Department of Geography, University of Liège, Liège, Belgium*
[e] *Geoinformatics Division, Department of Urban Planning and Environment, KTH Royal Institute of Technology, Stockholm, Sweden*

ARTICLE INFO

ABSTRACT

The assessment of cracks in civil infrastructures commonly relies on visual inspections carried out at night, resulting in limited inspection time and an increased risk of crack oversight. The Digital Image Correlation (DIC) technique, employed in structural monitoring, requires stationary cameras for image collection, which proves challenging for long-term monitoring. This paper describes the Crack Monitoring from Motion (CMfM) methodology for automatically detecting and measuring cracks using non-fixed cameras, combining Convolutional Neural Networks and photogrammetry. Through evaluation using images obtained from laboratory tests on concrete beams and subsequent comparison with DIC and a pointwise sensor, CMfM demonstrates accurate crack width computation within a few hundredths of a millimetre when compared to the sensor. This method exhibits potential for effectively monitoring temporal crack evolution using non-fixed cameras.

1. Introduction

Civil infrastructures include critical structures, such as bridges, tunnels, highways, and buildings. Many of these structures are becoming older and increasingly prone to severe failures that can lead to loss of lives and high economic costs. To prevent such infrastructure damage and failures, strict safety regulations for infrastructures have been recently defined. For this reason, administrators of infrastructures require more efficient monitoring systems to determine the health of tunnels, bridges, and other critical structures. Structural Health Monitoring (SHM) is one of the major approaches adopted to perform non-destructive evaluations of infrastructures [1]. Detection and measurement of cracks are essential SHM activities to ensure the structural capacity of concrete structures during their technical life span which is normally designed to be 100 years or more and can be achieved through recurrent monitoring, assessment and maintenance. Mostly, cracks are associated with concrete degradation and reinforcement corrosion which reduce the structural capacity. The extent of cracks constitutes, therefore, a key parameter in evaluating the safety and durability of structural components [2–4]. For this reason, cracks should be detected as soon as possible and monitored over time.

Nowadays, large civil infrastructures are routinely inspected to detect and measure cracks and to estimate the associated risk. Traditionally, this work is accomplished through visual inspection by experienced workers. However, this procedure is time-consuming, expensive, and prone to human errors. Furthermore, many of the monitored areas are difficult to reach or dangerous for standard inspection, which means that the severity of the cracks must be judged from the ground or using mobile platforms. Moreover, the service these infrastructures provide must often be interrupted to ensure the safety of inspectors. To minimize the impact of infrastructure downtime, inspections are usually carried out at night for a limited time. This aspect, combined with the length/width of the infrastructure to monitor, makes it very difficult and sometimes practically impossible to inspect the infrastructure in detail, increasing the risk that potentially dangerous cracks are not detected. Also, conventional devices for deformation and crack measurements, such as strain gauges, Linear Variable Differential Transducers (LVDT), and Fibre Optic Sensors (FOS) can provide only locally accurate information, limited to the area of the structure where they are installed [5].

In the last decades, different non-contact techniques for infrastructure monitoring, such as Digital Image Correlation (DIC), have been widely investigated to overcome the main drawbacks related to

---

visual inspection and standard devices [6–10]. With 2D DIC, a fixed camera can monitor in-plane displacements and strains by tracking the movement of individual pixels in time series of co-registered images. Yet, for long/wide infrastructures, the area that can be monitored with this technique is limited since the permanent camera setup is usually not suitable for long-term infrastructure monitoring and is difficult to ensure outside the controlled laboratory conditions.

Nowadays, cameras can be easily placed on vehicles or drones, enabling an automatic collection of infrastructure imagery from different points of view. An important objective of inspections is to determine whether or not the length and width of the cracks have propagated since the last inspection [11]. However, due to the limitations of standard 2D DIC, crack propagation cannot be measured from images collected from different points of view since in these cases the position of the camera between the inspections differs. Therefore, the information from the images collected using mobile mapping systems can only be adopted to generate a digital representation of the infrastructure (the so-called digital twin), detect the defects, and manually compare the features of the cracks between different inspections. Due to the large amount of collected data, this approach is still time-consuming, inefficient, and affected by human errors [12].

This study presents a novel algorithm, *Crack Monitoring from Motion (CMfM)*, which integrates photogrammetric techniques with deep learning methods for the automatic detection and monitoring of cracks. *CMfM* uses a series of images collected by non-fixed cameras to monitor the crack propagation over time. Unlike conventional techniques, *CMfM* is entirely automatic, does not require fixed artificial targets or un-deformed regions within the images and overcomes the 2D DIC limitations of using a fixed camera. Therefore, our methodology opens up new possibilities for automatically monitoring crack propagation using images collected with mobile mapping systems in long infrastructures such as tunnels and bridges. The widespread adoption of *CMfM* can hence lead to significant improvements in structural health monitoring and maintenance. The approach employs Convolutional Neural Networks (CNNs) for automatically detecting the shape of the cracks and a skeletonization approach for delineating the centre line of the defects and for automatically selecting the points of interest around the cracked area. Then, it computes the change in the distance between the selected points on the left and right sides of the crack for estimating the crack width propagation over time. The proposed approach is based on homography estimation and template matching techniques.

The paper is organized as follows: Section 2 gives a description of the available sensors and techniques for crack monitoring; Section 3 presents the proposed methodology; Section 4 describes and discusses the results from laboratory tests in which we measure the crack propagation in concrete beams with *CMfM*, the standard DIC technique and a pointwise LVDT; Section 5 outlines some conclusions and future prospects. Finally, the Appendix presents the results of different simulations performed using synthetic data to assess the methodology under ideal conditions.

2. Techniques for crack monitoring

2.1. Standard measurement techniques

Several devices have been extensively tested to study the fundamental physics of structural behaviour. Among them, strain gauges, LVDT, and FOS have been widely applied to investigate the deformation mechanism of structural elements subjected to loading systems. The LVDT measures the displacements in a specific direction. Strain gauges and FOS measure the strains and they can be adopted in continuous monitoring systems where several sensors are linked to a control unit. However, this approach can be highly invasive for the infrastructure since electrical or fibre optic cables need to be placed to make connections [13].

As regards standard crack measurements, different approaches can be adopted depending on the required accuracy, precision and cost of the monitoring system. For standard infrastructure inspections (Fig. 1(a)), graduated cards provided with a set of different thickness lines (Fig. 1(b)) are normally used to visually estimate the crack width [13].

Fig. 1. Visual inspection (a) using graduated cards (b).

This method gives a rough estimation of the crack features (width and length) at the specific time of the inspection but it is subjective and difficult to follow up over time. The movement of cracks could vary due to seasonal effects such as temperature and load conditions. It is, therefore, important to monitor the variation of crack features over time to understand how cracks affect structural behaviour.

Strain gauge, LVDT and FOS have been widely investigated for crack measurements. Independently from the adopted device, a common feature is the possibility to measure displacements/strains only along specific directions, which must be decided in advance before installing the instrument. These devices are more expensive than manual inspection but they can provide higher accuracy and objectivity. Strain gauges and LVDT have long been used to monitor the structural response of specimens in the laboratory [5,14] and on existing structures [15,16] since they usually provide reliable measurements. The sensors need to be attached to the surface of the investigated material and connected by wires to a data logger to record the measurements (Fig. 2).

Fig. 2. Strain gauge (a) and LVDT (b) sensors.

The basic principle of these sensors is to measure the change in electrical resistance caused by displacement. However, measurements are only provided at the location of the sensors, which require direct contact with the surface. For this reason, the number and placement of the adopted devices should be carefully planned before testing to get useful results. Furthermore, these sensors are sensitive to temperature, which needs to be taken into account through the simultaneous measurement of the air temperature. Then, the effects of temperature variations can be removed by considering the specific thermal expansion coefficient of the material inside the sensor. Finally, these devices are sensitive to electromagnetic fields which can disturb the signal of the instruments. For measurements of concrete materials, strain gauges are usually adopted in the laboratory to monitor the structural response of a material subjected to a loading system. The aim is to retrieve the rheology of the material (e.g. strength, elasticity, plasticity, and fatigue) and increase the understanding of its behaviour. Also, the measured

data can be used to verify or update numerical models. One of the benefits of strain gauges is that the sensor can be attached to reinforcement bars embedded in the structure and thereby measure the interior strain. Unfortunately, according to Leung [17] cracks have a small effect on the stiffness of the structure in reinforced concrete. For this reason, the strain gauges must be placed very close to the crack to capture any structural effects due to cracking. To measure the propagation of cracks in the concrete, the LVDT sensor is normally considered more reliable and suitable during laboratory tests. The LVDT is composed of two metal plates, which need to be glued to the surface on each side of the crack. Then, the distance between the two elements is measured during the deformation to retrieve the crack width. This type of instrument is easy to use but it presents different drawbacks. First of all, the exact location of the crack must be known before installing them. This is, of course, a strong limitation, especially outside the controlled laboratory conditions of specific tests (i.e. notched beams). Furthermore, the LVDT performs the measurement only along a fixed length and direction and, as well as strain gauges, can be damaged during destructive tests [18]. Finally, when long infrastructures need to be monitored, the procedure is time-consuming and not always allowed, especially in the case of historical or inaccessible structures [13].

Today, different types of FOS are available and capable of measuring strain, pressure, and temperature in civil engineering structures. The operating principle is based on measuring the changes in light properties. By coupling an optical fibre to a structure and monitoring the change in light intensity, phase, or wavelength at the output, information on the structural condition can be deduced. A FOS enables to overcome the limitation of strain gauges related to the temperature as they measure temperature and strain at the same time. Furthermore, a single FOS can be used to measure both the axial and transverse strains and it is not affected by electromagnetic interference since no electric current passes through them. Compared to standard point sensors that can detect changes only at specific locations, FOS for distributed sensing of cracks can be adopted. Among them, Fibre Bragg Grating (FBG) allows for strain measurements at multiple locations and provides more extensive information [17]. Unfortunately, their use in long infrastructure systems is still limited since they are more expensive than their electrical counterpart and they present some practical problems. One of them is related to the placement and alignment of the cable which must be connected to the concrete to be able to detect and measure the width of cracks. This can be achieved by glueing the cable on the surface of the concrete, but that makes it vulnerable to damage. An alternative solution is to attach the cable to the reinforcement and embed the cable in the concrete. However, there is a risk that the cable is damaged or detached from the reinforcement during concreting. Regarding the application of FOS for crack monitoring in concrete, it is worth mentioning the approach presented by Bremer et al. [19]. The principle of their crack detection system is to attach the device to a textile structure embedded in the concrete. In this way, the displacement of the concrete is, through the textile structure, enforced to the FOS which breaks at small crack sizes (1.4 mm in the performed test). The position of the crack can then be determined with an optical time-domain reflectometer [19].

Overall, graduated cards, strain gauges, LVDT and FOS can provide relevant and accurate (at different levels) measurements for crack monitoring, but only in pre-selected locations and directions. They require permanent installations onsite and they can provide very limited flexibility to follow the evolution of the cracks over time.

2.2. Image-based techniques

Image-based techniques, different from the described standard ones, can simultaneously address the problems of crack delineation and measurement. In this respect, different image-based approaches for crack monitoring have been widely developed, representing a promising

alternative to visual inspection and standard devices. Image binarization is the simplest image processing technique currently employed to perform crack delineation and measurement. Cracks are usually darker than their surrounding area since they are characterized by low-intensity values compared to the background. For this reason, thresholding techniques have been widely investigated to segment the shape of the crack and extract its features. However, the use of this type of method (e.g. the Otsu thresholding [20]) is not accurate enough since it strongly depends on the binarization parameters, the image quality, the background characteristics and the change in lighting conditions [2]. Regarding the choice of the optimal parameters, Kim et al. [21] performed a parametric analysis to determine the optical parameters of five different binarization methods. They also proposed a comparative analysis of these techniques for crack delineation and measurement in concrete structures.

To enhance binarization method performance, the combination with other techniques has also been extensively explored. Sohn et al. [22] proposed a crack monitoring system using different image processing techniques including image enhancement, noise removal, histogram thresholding, and thinning for crack linear feature extraction. Ito et al. [23] explored the combination of shading correction, thresholding and thinning. Similar methods were also presented in [24] and [25]. Yu et al. [26] adopted image processing techniques combined with a semi-automatic mobile system for tunnel inspection and crack measurement. Zhang et al. [27] utilized morphological image processing techniques combined with thresholding operations and Extreme Learning Machine classifiers to perform image segmentation, feature extraction and crack classification. They also proposed an algorithm for crack quantification based on the skeleton graph to calculate the crack length and width. Yamaguchi and Hashimoto [28] combined a high-speed percolation method with binary and dilation processing, shading correction, erosion and thinning processing to extract cracks on concrete surfaces. They developed an image-based method for crack measurement with sub-pixel accuracy in real concrete structure applications [29].

In addition to binarization methods, other techniques have been widely investigated. Dare et al. [30] proposed a bilinear interpolation method for crack width measurement with sub-pixel accuracy. However, the approach required human intervention for feature extraction and could only provide pixel measurements. Later, Chen et al. [31] improved the approach using quadratic curve interpolation. Dias-da Costa et al. [32], Valença et al. [33] proposed a combination of photogrammetry and image processing for computing the strain field and mapping the cracked areas. The processing was almost completely automatic but it required a regular grid of circular targets painted on the sample that could be affected by imperfections and discontinuities of the concrete surface. Barazzetti and Scaioni [13] presented the IMCA (IMage Crack Aperture) tool for crack border and width extraction based on the behaviour of the RGB component intensity along cross-sections of cracks. Finally, deep learning techniques (Convolutional Neural Networks — CNNs) have been recently investigated to automatically detect the shape of the cracks [34–39]. CNNs represent powerful techniques for automatic feature extraction and classification problems. They are designed to automatically and adaptively learn spatial hierarchies of features through backpropagation by using convolution layers, pooling layers and fully connected layers. Starting from a set of labelled images for training the network, CNNs can be adopted to build a classifier for automatically detecting objects (e.g. cracks) in new images. Among the developed approaches, semantic segmentation provides pixel-level classification by detecting all the pixels that belong to the crack and this approach represents the most accurate method for the specific task of crack detection [38]. In particular, the U-Net architecture is the most adopted in the field of semantic segmentation [40].

Among image-based approaches, the optical DIC technique has also been extensively used as a standard method to measure displacements, strains and crack propagation when high accuracy is required [14,41–43]. The 2D DIC technique provides in-plane full-field displacements

and strains over large areas without the need for direct contact with the structural element to monitor. Moreover, compared to standard techniques, 2D DIC is less expensive and easier to use especially if larger areas need to be monitored since it requires only a camera to acquire the images and natural light for illuminating the scene. The typical 2D DIC acquisition system is composed of a planar sample connected to a loading system, a standard camera to acquire the images and a computer to process the recorded images (Fig. 3).
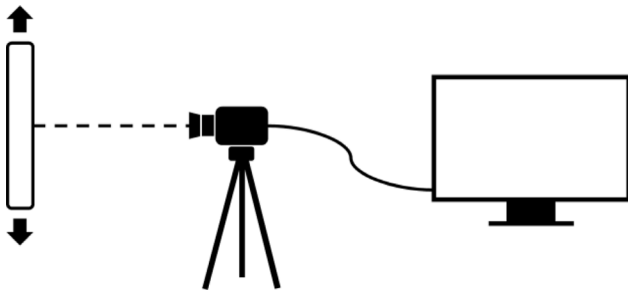
Fig. 3. Example of image acquisition system of 2D DIC.

The method uses a simple experimental setup and sample preparation, especially if the specimen surface has a natural texture characterized by a random gray intensity distribution which is normally ensured by the texture of materials such as concrete [10]. In some cases, a speckled pattern is sprayed on the surface to improve the performance of the technique. Even if 2D DIC presents lots of advantages, three requirements need to be satisfied to accurately estimate the displacement fields from the images:

- the camera position must be kept fixed during the entire acquisition since the displacements are directly extracted from the images;
- the sample must be characterized by a flat surface, the optical axis of the camera should be kept perpendicular to the flat surface and out-of-plane displacements should be small enough to be neglected;
- the imaging lens system should not be affected by geometric distortions to avoid additional displacements due to distorted image coordinates [10]. If the effect of geometric distortions cannot be neglected, camera calibration models [44,45] should be used.

It is worth mentioning that different studies have been carried out to understand the effects of lens distortion, out-of-plane motion and non-parallelism between the image plane and the object surface [46–49]. In Feng et al. [46] the authors underlined that even significant misalignments up to 5 degrees with respect to the parallelism condition have a very small impact (within 0.5%) on the estimated displacement.

Nowadays, two different DIC approaches for full-field kinematic measurements are available: the subset-based DIC (local DIC) and the finite element-based DIC (global DIC) [50]. Local DIC compares the gray intensity changes of a sample surface in the un-deformed (or reference) and deformed states, respectively. Specifically, it computes displacement and strain fields by correlating each subregion of the Area Of Interest (AOI) at different levels of deformation to the corresponding subregion at the reference stage. Thus, subset-based DIC processes each calculation point independently, without applying displacement continuity to the global displacement fields [51]. This procedure is performed by tracking the pixel inside the AOI using matching algorithms (Fig. 4).

Global DIC, conversely, usually discretizes the AOI using finite element mesh and then tracks all these elements in the target image simultaneously. In this way, displacement continuity can be explicitly ensured between adjacent elements by the shared nodes [14].
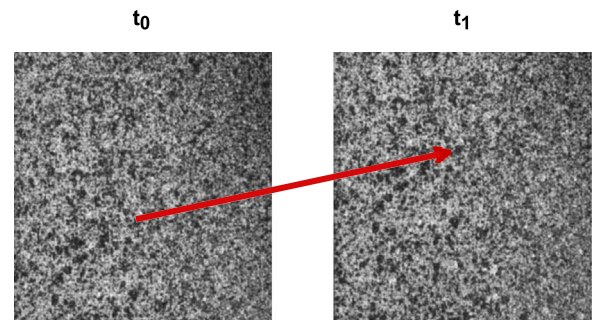

Fig. 4. DIC pixel tracking.

As regards crack monitoring, both local and global approaches have been widely investigated [43,52–60]. Usually, when a crack appears in the acquired images and the DIC technique is adopted, a sudden jump in the displacement fields can be detected. Therefore, starting from the DIC displacement fields, the crack width can be computed to study the failure mechanism of concrete or other materials. It is important to underline that when complex or multiple cracks occur, modified DIC techniques should be taken into account to improve the performance of the method. Fagerholt et al. [61] proposed a modified global DIC approach using an adapted mesh with node splitting to improve the methodology and capture discontinuous displacement fields or complex phenomena. Helm [62] modified the local Newton Raphson-based DIC process to automatically analyse specimens with multiple growing cracks that can be difficult to measure with standard DIC.

Thanks to its simplicity and its advantages over standard techniques, the DIC method has been extensively adopted in controlled laboratory environments to perform measurements during experimental tests (Fig. 5(a)). However, even if the technique is powerful and easy to use, the need for a fixed camera represents a constraint that strongly limits the use of DIC outside the controlled lab environment. For measurements over a long period, the position of the camera could be difficult to secure, especially in case of wind, vibrations or ground instability. In this scenario, one possible solution is to identify and filter the displacements related to the frequencies of the camera movement using triaxial accelerometers mounted on the camera. However, this method can only be adopted if the camera and the structural motion frequencies are not similar. A different solution is to directly subtract the motion of a static object/scene in the images from the total motion [63,64]. Furthermore, for large civil infrastructures, a fixed camera can only be used to measure displacements, deformations and crack movements in a few critical sections (Fig. 5(b)).
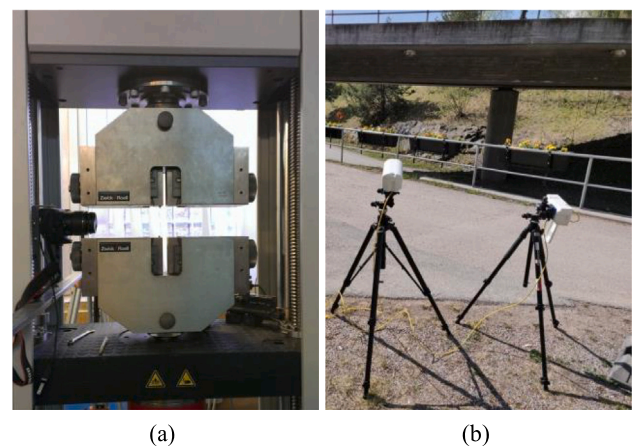

(a)   (b)

Fig. 5. DIC setup inside (a) and outside (b) the controlled laboratory conditions.

Therefore, the procedure of crack monitoring on concrete structures by quantifying the changes detected from multi-temporal images allows to delineate and consider the whole crack, overcoming the limitation of monitoring pre-selected locations/directions only. Nevertheless, the camera installation requirements at fixed locations represent, also in this case, a strong practical limitation for image-based techniques. For this reason, to monitor the long-term deformation or propagation of cracks in bridges or tunnels, a moving camera (also mounted on mobile mapping systems or drones) is the most feasible option. In this case, image acquisition can be performed at different epochs and the camera can be removed and replaced between each measurement, releasing the acquisition constraints and reducing the effects of environmental conditions. However, if the camera is removed and replaced during the acquisition period, the position and attitude of the camera differ at each time and the image coordinates change in all the acquired images. Therefore, when using portable cameras, the images include not only the deformation of the surface but also the effect of the camera movement. To remove this effect, static areas inside the images are normally required. The problem is then solved by using the perspective transformation which describes the relationship between un-deformed points (usually manually marked points) on the images acquired before and after the camera movement. The unknown coefficients of the transformation are estimated using the least squares method starting from a coordinate set of fixed points. Finally, once the transformation coefficients are estimated, the effect of the camera movement is removed and the deformation or the crack propagation is computed. Using the approach based on perspective transformation, Yoneyama and Ueda [64] leveraged fixed reference regions on both sides of a bridge to remove the effect of camera movement and measure the bridge deflection. Adopting a similar approach, Sohn et al. [22] proposed a crack monitoring system. They used targets with known image coordinates and object space coordinates to estimate the projective transformation and create the reference crack coordinates in the object space. Then, they transformed the crack image coordinates of each image acquired with a moving camera into the same object coordinate of the real surface using a modified iterated Hough transform algorithm. They combined the procedure with image processing techniques to detect and quantify the change of cracks on the concrete surface. Similarly, Nishiyama et al. [65] placed reflective targets along both sides of cracks in a concrete tunnel to measure their propagation over time using non-fixed cameras. Specifically, they converted digital images acquired from arbitrary positions to images facing the targets through the perspective projection and they finally computed the distance between the target centres to obtain the crack width over time.

To the best of our knowledge, the use of un-deformed regions, or targets, inside the images is the only solution currently available for the use of non-fixed cameras. However, un-deformed regions are hardly available inside the acquired images and difficult to identify automatically. Furthermore, considering the length of the infrastructure to monitor, the target setup is always time-consuming and not feasible since it requires the infrastructure to be closed down for traffic. There is also a potential risk of target falling during inspections, especially for long-term maintenance. For all these reasons, the approach based on fixed regions or targets represents a reasonable method only to monitor crack propagation during the construction period, or if a few small areas need to be monitored during a short period. For recurrent inspections, performed when the infrastructure is in operation, the logistic constraint to set up and maintain targets still represents a severe limitation, mainly for long/wide infrastructure. For all these reasons, we developed *CMfM* to detect and monitor the in-plane evolution of cracks through the analysis of a time series of images captured with non-fixed cameras. The methodology is described in detail in the following section.

3. Methodology

This section presents *CMfM*, the novel methodology we developed, tested and validated to release the 2D DIC logistic constraint related to the fixed position of the camera and bring the technique to a fully operational level for long-term infrastructure monitoring. The method is completely automatic and it does not require the presence of targets or un-deformed regions within the images. Therefore, it can be widely adopted for improving the efficiency and objectivity of structural monitoring.

The workflow of *CMfM* is divided into three main steps (Fig. 6):

- data collection;
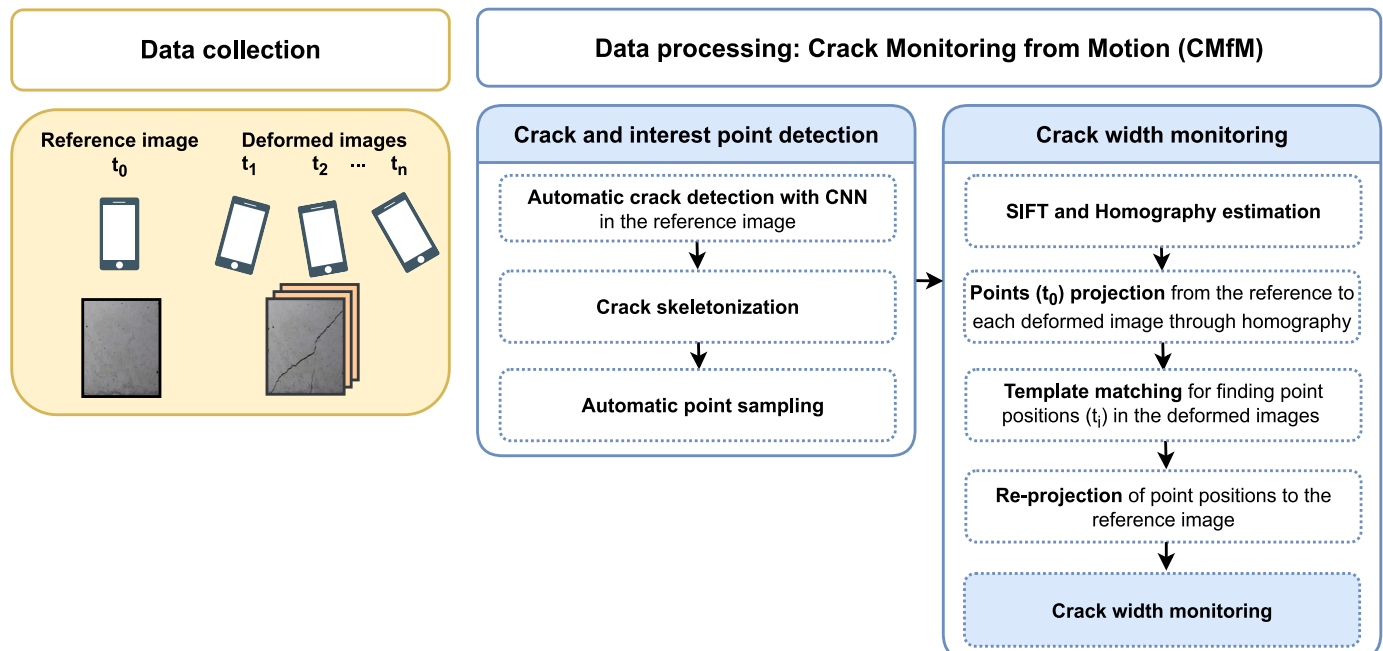- crack and interest point detection;
- crack width monitoring.

Fig. 6. *CMfM* workflow.

3.1. Data collection

The first step of *CMfM* is data collection whose aim is to capture a time series of images using non-fixed cameras. With our approach, standard commercial cameras or smartphones can be used to collect images of cracks at different levels of the deformation process (time $t_0, t_1, t_2, \ldots, t_n$). Usually, the first image is referred to as the reference image, while all the others are named deformed. The images can be acquired from different positions to capture the in-plane crack propagation during short-term and long-term monitoring. The proposed methodology focuses on measuring the in-plane crack propagation since planar surfaces are considered a good approximation for the majority of structural elements (e.g. beams or generic material samples of laboratory tests, pillars of bridges and tunnel lining), especially if the area of interest captured in the images is limited.

3.2. Crack and interest point detection

The second step of *CMfM* is the automatic detection of the crack of interest in the reference image $I(t_0)$. For this purpose, we used a semantic segmentation approach, implementing a U-Net segmentation network [40] combined with different backbones (e.g. Visual Geometry Group [66] — VGG 16 and VGG 19) using pre-trained weights from ImageNet [67]. We developed the processing pipeline within the Google AI platform using Keras-TensorFlow and Segmentation Model libraries. For training the U-Net segmentation network, we used a subset of a dataset available online [68] containing around 11.220 images (448 × 448 pixels) and corresponding crack annotations merged from different available crack segmentation datasets [69–74]. This dataset includes indeed cracks with different scales and cracks related to completely different scenarios: ideal cracks, crack-similar-looking objects, cracks on a noisy background and cracks covered by moss [75]. In the present work, we considered only the cracks related to the most interesting cases for crack detection in concrete materials, selecting around 2500 images and the corresponding annotations. We performed data augmentation using the Albumentation Python library [76] to virtually increase the size of the dataset and make the neural network more robust. Specifically, we applied a horizontal flip of the images around the *y*-axis with a probability $p = 0.5$, a combination of scaling ($max = 0.2$), rotation ($max = 20°$) and shifting ($max = 0.1$) of the images with a probability $p = 1.0$, and a random crop of part of the images with a probability $p = 1.0$. We trained the network using 80% of the imagery in the dataset for 80 epochs (batch size = 4) with a learning rate of 0.00001 and a reducing learning rate on the plateau. We used a combination of dice and binary-focal loss functions and the Adam optimizer [77]. We used the remaining 20% of the imagery as the test set to assess the network performances. During testing, we set a fixed threshold of 0.5 to obtain binarized segmentation images from the probability maps. Then, we computed five common segmentation accuracy metrics for the quantitative accuracy assessment: Accuracy (A), Intersection over Union (IoU), Precision (P), Recall (R) and F1 score (F1). Formulas for the metrics are given in the following equations, where TP are true positives, TN are true negatives, FP are false positives, and FN are false negatives:

$$Accuracy = \frac{TP + TN}{TP + FP + FN + TN}$$

$$IoU = \frac{TP}{TP + FP + FN}$$

$$Precision = \frac{TP}{TP + FP}$$

$$Recall = \frac{TP}{TP + FN}$$

$$F1 = \frac{2PR}{P + R}$$

In particular, we calculated the standard metrics for each image and then we aggregated the values using the medians and standard deviations for each metric.

Figs. 7 and 8 show the results achieved using the U-Net architecture combined with the VGG 16 backbone. Fig. 7 presents the loss and F1 curves for training and testing; Fig. 8 shows the segmentation accuracy metrics on the test set.

In our approach, we first apply the trained model to the reference image (Fig. 9(a)) to detect the crack (Fig. 9(b)). Then, we use a skeletonization algorithm to delineate the centre line of the identified crack (Fig. 9(c)). Finally, we automatically select N sections along the crack skeleton (Fig. 9(d)) identifying pairs of points on the left and right sides of the crack. These points identify the locations where the crack width propagation is measured using the methodology reported in the following section.

3.3. Crack width monitoring

The third step of *CMfM* is the automatic crack width monitoring. This step is based on the Scale-Invariant Feature Transform (SIFT) algorithm that is used to automatically match corresponding features in all the collected images even with variations in scale and viewpoints [78]. The SIFT matched points are adopted to estimate the homography transformations (H_{0i} with $i = 1, \ldots, n$) representing the camera movement between the reference image $I(t_0)$ and all the n subsequently acquired deformed images $I(t_i)$ with $t_i > t_0$ and $i = 1, \ldots, n$ (Eq. (1)).

$$
\begin{aligned}
&I(t_0) \underset{H_{10}}{\overset{H_{01}}{\rightleftarrows}} I(t_1) \\
&\quad\vdots \\
&I(t_0) \underset{H_{i0}}{\overset{H_{0i}}{\rightleftarrows}} I(t_i) \\
&\quad\vdots \\
&I(t_0) \underset{H_{n-1 0}}{\overset{H_{0n-1}}{\rightleftarrows}} I(t_{n-1}) \\
&I(t_0) \underset{H_{n0}}{\overset{H_{0n}}{\rightleftarrows}} I(t_n)
\end{aligned}
\tag{1}
$$

If a crack appears in the images, the homography is automatically estimated using only the points on one side of the crack (Fig. 10).

CMfM can adopt two robust methods instead of a simple least-squares scheme for estimating the homographies. In this way, the algorithm uses only the good matches or the so-called inliers to provide the correct homography estimation. The two used robust methods are RANdom SAmple Consensus (RANSAC) [79] and Least Median [80]. Such methods test many different random subsets of the corresponding point pairs (of four pairs each for the homography computation) and estimate the homography matrix using the selected subset and a simple least square algorithm. It is worth mentioning that RANSAC can handle any ratio of outliers but it needs a threshold to distinguish inliers from outliers. On the other hand, the Least Median method does not need any threshold but it works correctly only when there are more than 50% of inliers. The quality of the computed homography is evaluated through the number of inliers for RANSAC and the median re-projection error for Least Median. The best subset is used to produce the initial estimate of the homography matrix and the mask of inliers. Finally, the computed homography matrix is refined using all the inliers with the Levenberg–Marquardt algorithm to reduce the re-projection error [81, 82].

Once the homography is estimated for each image pair (Eq. (1)), the points of interest automatically selected in the reference image $I(t_0)$ (Fig. 11(a)) are projected from the reference image to each one of the n deformed images using the estimated homographies H_{0i}. Then, *CMfM* adopts the selected points on the reference image and the projected points on each deformed image to perform a template matching procedure and compute the displacements of the points of interest caused exclusively by the deformation of the monitored object. Through the approach implemented in *CMfM*, indeed, the homography
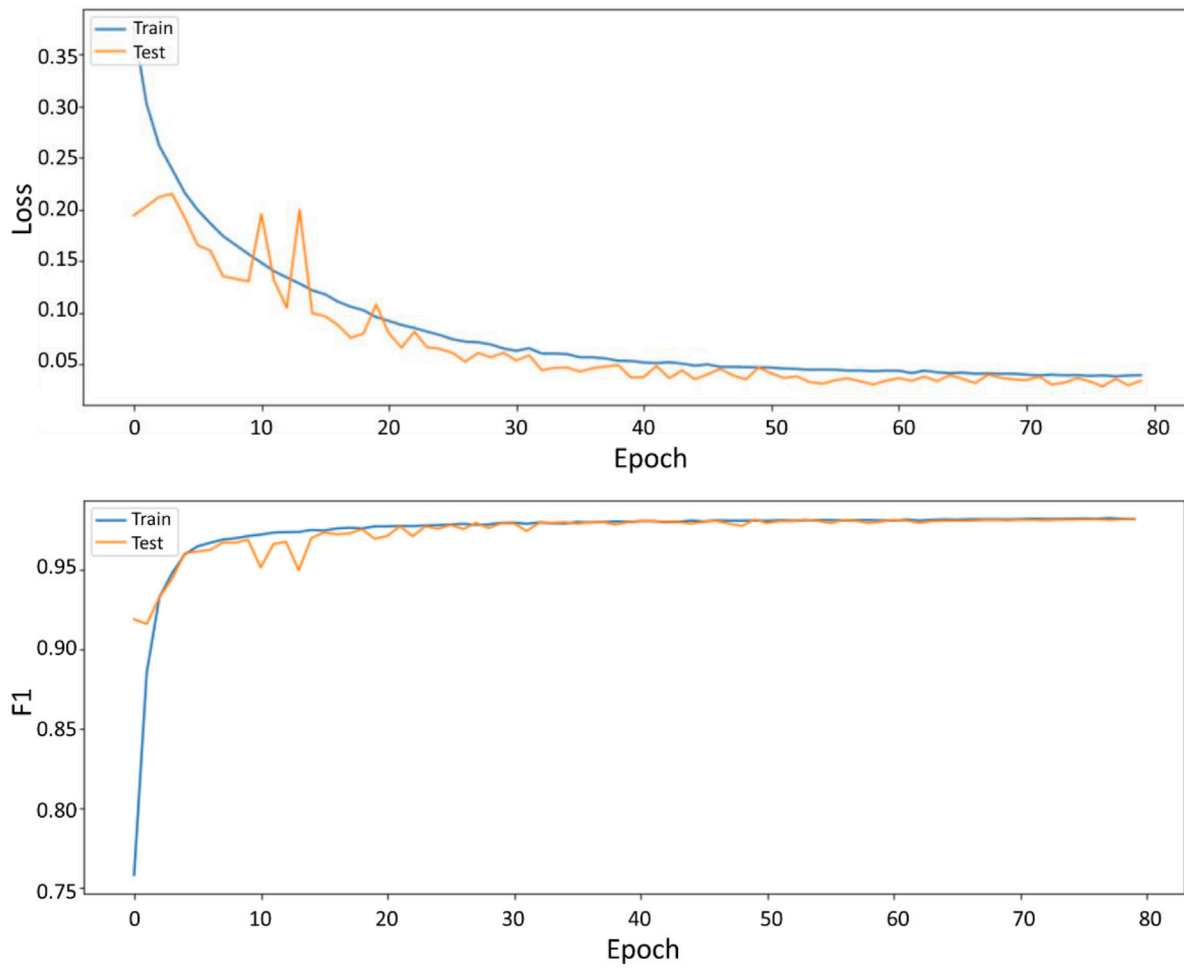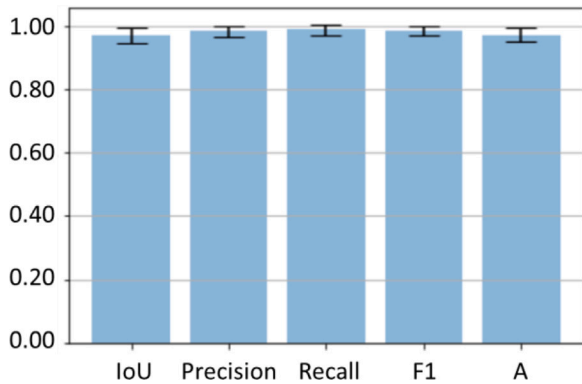
Fig. 7. Loss and F1 score training curves.

Fig. 8. Computed metrics (medians and standard deviations) on the test set.

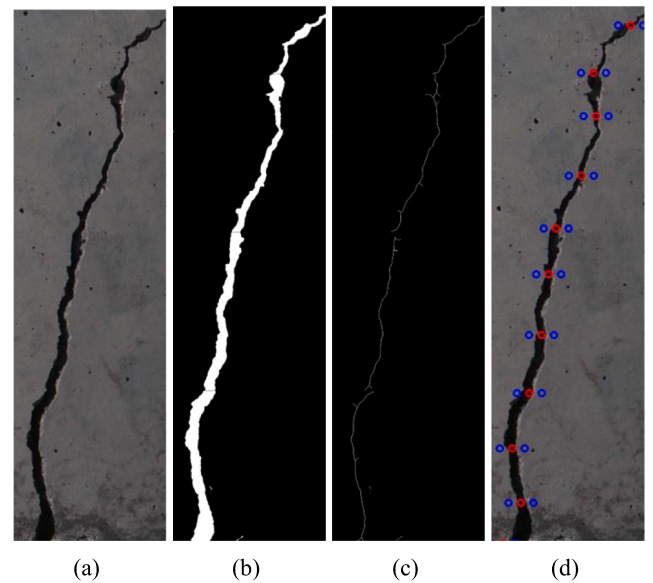(a)   (b)   (c)   (d)

Fig. 9. Original image (a), automatic crack detection (b), crack skeletonization (c) and automatic point sampling (d).

between each image pair is firstly estimated and then applied to the selected points. In this way, the computed displacements do not include the effect of the camera movement but only the effect of the crack propagation. At the end of the processing, the positions of the points of interest in the deformed images (time t_i) obtained through the matching step are re-projected back on the reference image using the inverse homography matrices H_{i0}. The aperture of the crack is then computed
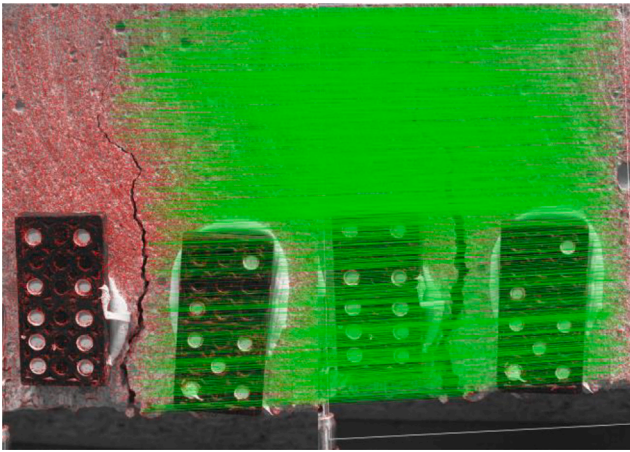
Fig. 10. Homography estimation between the reference image $I(t_0)$ and one of the deformed images $I(t_i)$.

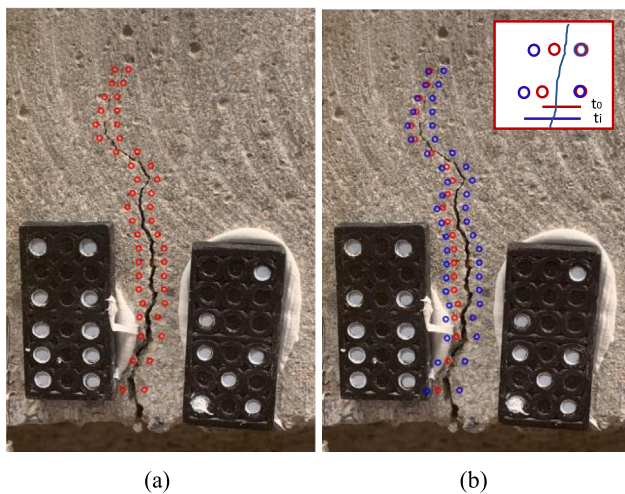(a)   (b)

Fig. 11. Automatically selected points (t_0 — red) in the reference image (a) and re-projected points (t_i — blue) from the deformed to the reference image (b).

on the reference image as the difference of the distances between the initial pairs of points (time t_0 — red in Fig. 11) and the re-projected point positions (time t_i — blue in Fig. 11) of each deformed image. All the measurements are, therefore, carried out on the reference image. This is the reason why our approach does not need information on the spatial resolution for each camera position, but only the spatial resolution of the reference image. Therefore, the only requirement of our methodology is a reference scale at the reference stage (time t_0) which is used for computing the pixel dimension and estimating the scale. It is also worth highlighting that our approach applies the estimated homography only to the points of interest and not to the entire images. In this way, we avoid reprojecting and resampling the images preserving the original texture information.

4. Results

We tested the performance of the proposed methodology by processing the data collected during two different laboratory tests. Firstly, we tested *CMfM* on images acquired with an iPhone XS placed close to the cracked area (from a distance of about 10 cm) of a concrete beam subjected to loading. Then, we investigated a more challenging dataset of images acquired with an iPhone SE from a higher distance (around 35 cm). The two datasets are available on Mendeley Data [83,84].

4.1. Experimental test 1

The aim of the first case study was to measure the crack propagation in a concrete beam using *CMfM* and compare the results with the measurements obtained employing the standard 2D DIC and an LVDT. The setup consisted of a $800 \times 150 \times 100$ mm (length $\times$ width $\times$ height) post-tensioned concrete beam subjected to three-point bending (Fig. 12).
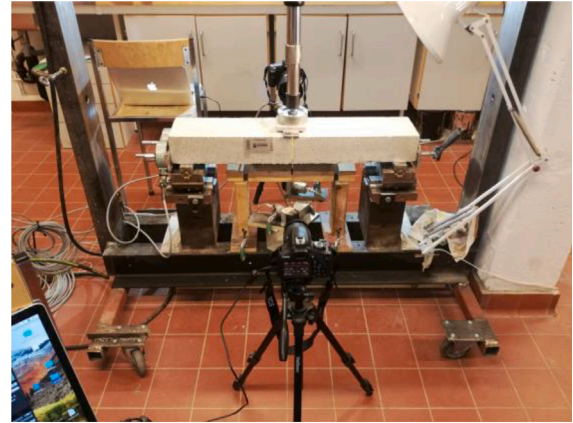

Fig. 12. Laboratory setup for the three-point bending test.

Before testing, we placed two 3.4 mm steel bars in the plastic tubes and post-tensioned them to approximately 18 kN. We applied an external load of 1.5 kN to prevent crack generation at the top of the beam during post-tension. No internal structural connection existed between the steel and the concrete. This setup normally yields the development and controlled propagation of one single and centric-placed crack.

To collect the data, we adopted three cameras and we installed an LVDT on one side of the beam. We placed the devices according to the following scheme:

- side A - a Canon EOS 2000D (22.3×14.9 mm CMOS sensor, 24 Megapixels, pixel size of 3.72 μm) fixed on a tripod during the entire test at a distance of 45 cm and an iPhone XS camera (12 Megapixels) manually moved between each acquisition at a distance of around 10 cm (Fig. 13(a)).
- side B - a Canon EOS 5D Mark 2 (35.8×23.9 mm CMOS sensor, 21.1 Megapixels, pixel size of 6.41 μm) at a distance of 50 cm mounted on a tripod and moved between each load step to acquire images from slightly different positions, and an LVDT (range of 10 mm and a displacement measurement over a distance of 144 mm) placed at the bottom and centre part of the beam (Fig. 13(b)).
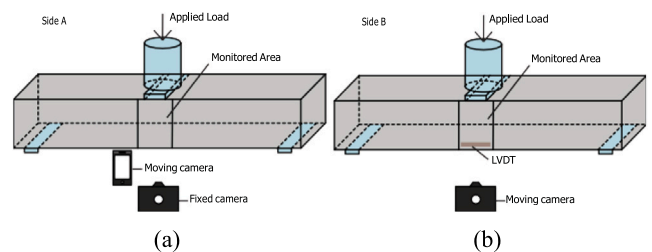

(a)   (b)

Fig. 13. Instrument setup on side A (a) and side B (b).

During testing, we applied the load according to a fixed scheme. At the beginning of each step, we increased the load by 1 kN and we maintained it constant during the entire interval. The LVDT recorded the horizontal displacements during all the steps. For each load step, we acquired three images on both sides of the beam using the fixed and

moving Canon cameras. Before cracking, we acquired all the images on side A using only the fixed camera (Fig. 14(a)). On side B, we captured the first image of each step using a fixed position, then we rotated and translated the camera before acquiring the second and third images (Figs. 14(c) and 14(d)).
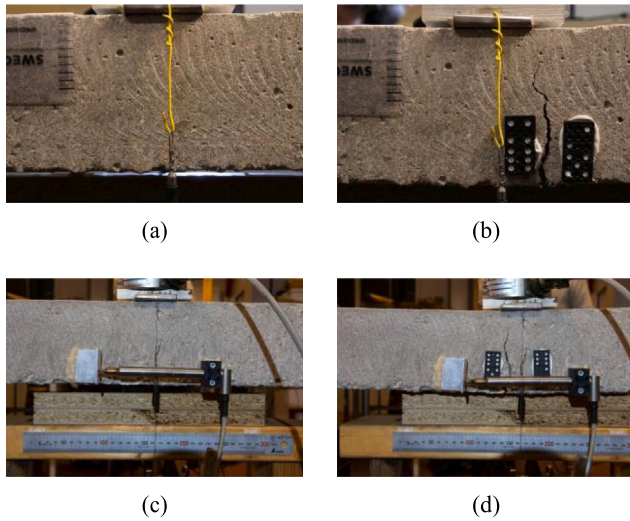

(a)　　　　　　　　(b)

(c)　　　　　　　　(d)

Fig. 14. Images collected on side A (a, b) and side B (c, d) using the Canon cameras.

After cracking, we adopted the Canon cameras according to the above-mentioned scheme and, on side A, we used the iPhone XS to acquire one image for each load step using slightly different camera poses. Fig. 15 shows examples of images acquired using the iPhone XS camera.
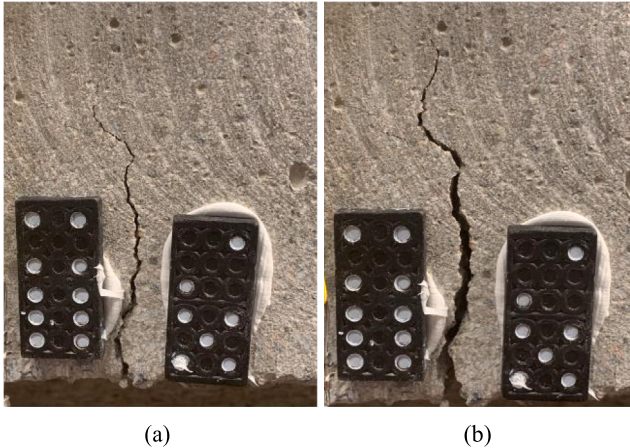

(a)　　　　　　　　(b)

Fig. 15. Images collected on side A using the iPhone XS at the time t_0 (a) and t_6 (b).

We carried out the comparison between the fixed and the moving cameras using the images acquired on side A with the fixed Canon EOS 2000D camera and the non-fixed iPhone XS cameras. In particular, we considered a series of six reference-deformed image pairs to monitor the crack propagation over time. Firstly, we automatically detected the crack in the reference image of the moving camera using the trained U-Net network and we identified the centre line of the defect using a skeletonization algorithm. Then, we automatically selected the points of interest at a defined distance from the skeleton on the left and right sides of the defect.

We processed the images acquired with the non-fixed camera adopting the RANSAC method with a threshold of 0.8 to estimate the homography between each of the considered image pairs. In this way, we reduced the impact of the outliers. We combined the reference

image $I(t_0)$ corresponding to the time t_0 with each one of the six deformed images ($I(t_i)$ with $i = 1, \ldots, 6$) acquired at different levels of the crack propagation ($t_1, t_2, t_3, t_4, t_5, t_6$). We projected the selected points of interest from the reference image to each one of the six deformed images using the estimated homography matrices. Then, we computed the displacement of each projected point of interest (filtered by the homography transformation) using the template matching algorithm considering a template of 51×51 pixels with an oversampling factor of 10 in the horizontal and vertical directions. At the end of the procedure, we re-projected the final positions of the points of interest (time t_i) from the deformed to the reference image and we computed the distance (in pixels) in the horizontal direction of each pair of the points of interest on the left and right sides of the crack. The difference between the initial distances (t_0) and the distances (t_i) computed after re-projecting the points on the reference image provided the crack aperture over time. The computation of the crack aperture in the reference image after point re-projection solved the problem related to the different spatial resolutions of each camera position. In this way, only the pixel dimension of the reference image $I(t_0)$ was required.

To compute the results of the fixed camera, we projected the automatically selected points from the reference image of the moving camera to the reference image of the fixed one through the homography transformation between the two images (Fig. 16). Again, we adopted the RANSAC method with a threshold of 0.8.
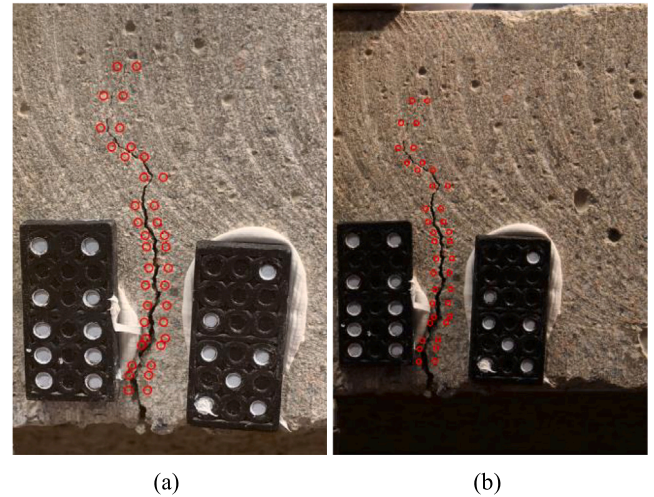

(a)　　　　　　　　(b)

Fig. 16. Projection of the selected points from the moving reference image (a) to the fixed reference image (b).

Then, we processed the images of the fixed camera with the local 2D DIC approach implemented in *Py2DIC*, an open-source and cross-platform Python software developed at the Geodesy and Geomatics Division of Sapienza University of Rome [14,85,86]. Based on the well-known template matching method, it computes 2D displacements and strains of a sample by comparing one or more image pairs of its surface acquired at different steps of the deformation process using a camera with a fixed position over time. Specifically, we used the points of interest (projected from the reference image of the moving camera to the reference of the fixed one) as centres of the templates in the template matching procedure performed through *Py2DIC*. Again, we computed the displacements using the corresponding six image pairs collected with the fixed camera using a template of 51×51 pixels and an oversampling factor of 10 in the horizontal and vertical directions. Starting from the displacements, we calculated the crack aperture for each pair of points on the left and right sides of the crack as the variation of the point distance in the horizontal direction, as done for the moving images. The comparisons between the crack aperture computed with the fixed and the moving cameras for each pair of points are shown in Figs. 17 and 18.
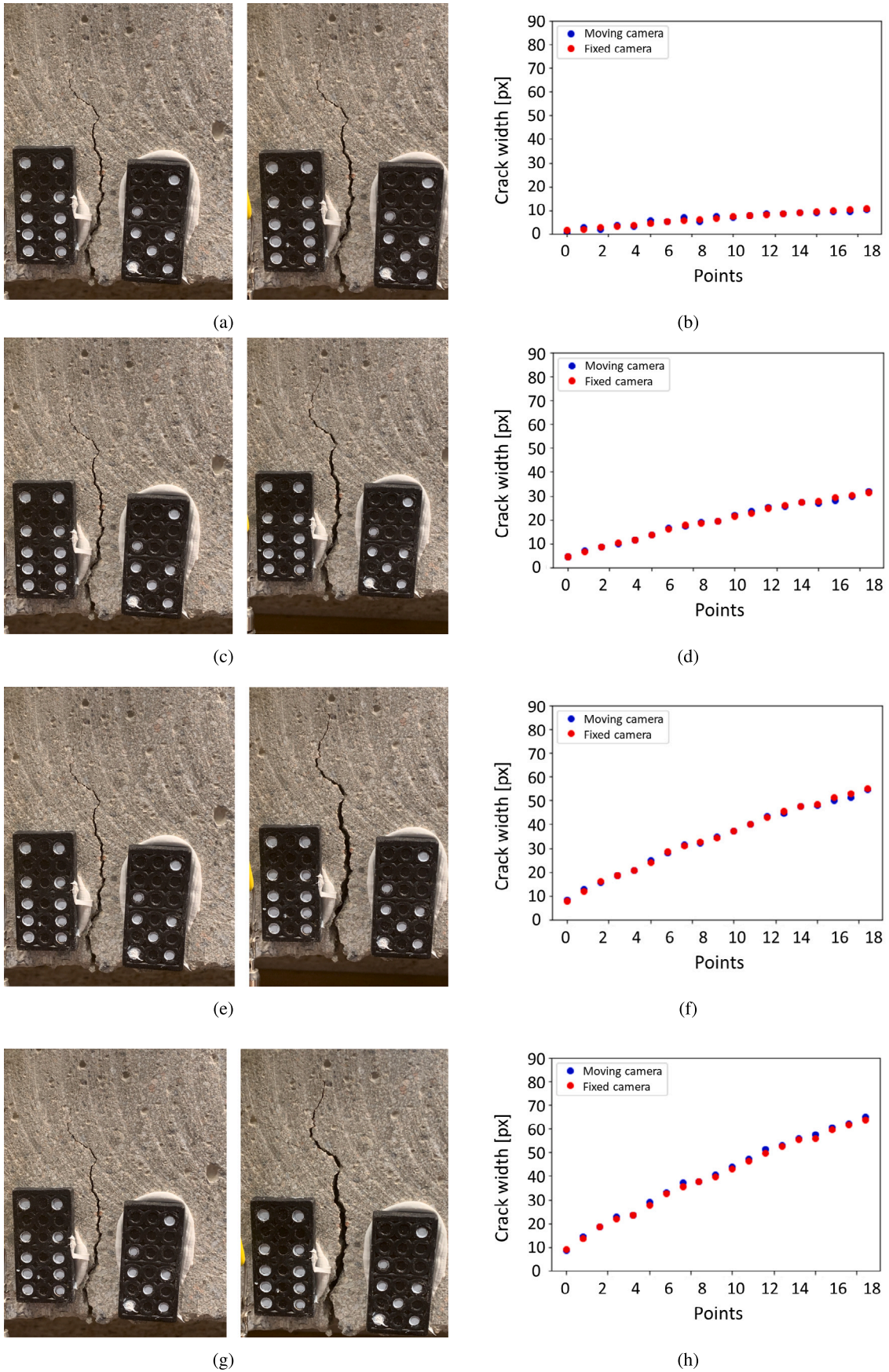
Fig. 17. Crack width comparison between *CMfM* and DIC $(t_0 - t_1, t_0 - t_2, t_0 - t_3, t_0 - t_4)$.
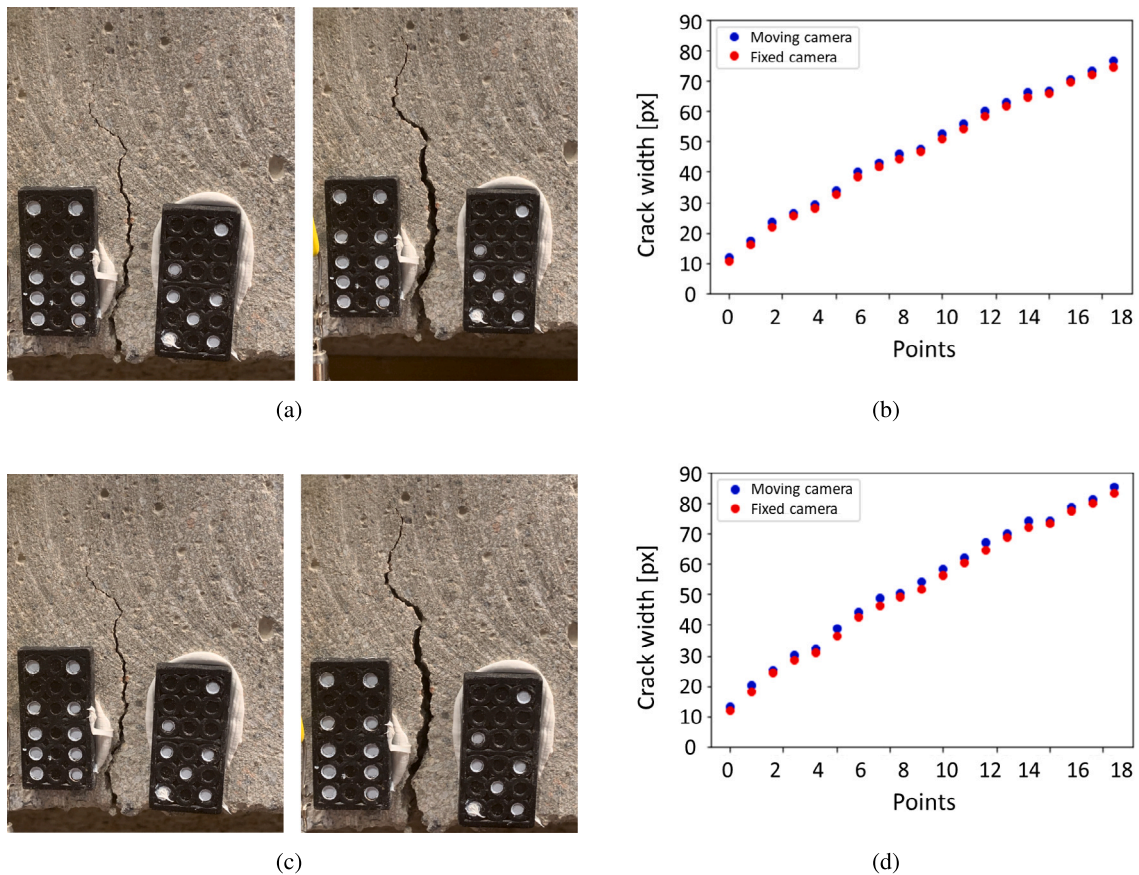
(a)

(b)

(c)

(d)

Fig. 18. Crack width comparison between *CMfM* and DIC ($t_0 - t_5, t_0 - t_6$).

Table 1 shows the mean, median, standard deviation and Normalized Median Absolute Deviation (NMAD) values of the differences between *CMfM* and *Py2DIC* for each step.

Table 1
Comparison between *CMfM* and DIC.

Step	Mean [px]	Median [px]	Std Dev [px]	NMAD [px]
$t_0 - t_1$	0.06	0.22	0.64	0.62
$t_0 - t_2$	−0.00	−0.16	0.50	0.40
$t_0 - t_3$	0.12	0.12	0.59	0.42
$t_0 - t_4$	−0.67	−0.82	0.55	0.65
$t_0 - t_5$	−1.38	−1.32	0.36	0.41
$t_0 - t_6$	−1.67	−1.76	0.52	0.73

The results highlight how the crack width computed using the moving camera and the *CMfM* approach well follows the reference trend of the fixed camera, at the level of one pixel which is equal to 0.026 mm in the reference image of the iPhone XS. It is worth mentioning that the optical axes of the first images of the moving and fixed cameras should be kept, in theory, perpendicular to the test surface. In the performed test we acquired the reference images as much as possible parallel to the sample surface and we neglected the effect related to small deviations to the perpendicularity condition. It is also worth noticing that the comparison is slightly worse in the last two steps (see Fig. 18). This is probably due to the fact that the images were not simultaneously acquired with the fixed and moving cameras; small differences in the comparisons are probably caused by displacement variations that can arise during each load step. This effect usually increases with the evolution of the crack.

On side B, we adopted the same methodology to process the images acquired using the moving Canon EOS 5D Mark 2 camera and we compared the crack aperture computed using *CMfM* with the data recorded by the LVDT. In this case, the *CMfM* results and the device recordings were not directly comparable since it was not possible to compute the displacement of the surface corresponding to the LVDT position due to the occlusion of the sensor. To solve this problem, we computed the crack width in the areas above and below the device and we applied a linear interpolation to obtain the crack aperture corresponding to the area covered by the LVDT (Fig. 19(a)). Then, we performed the pixel-to-millimetre conversion for a direct comparison with the LVDT measurements. To estimate the pixel dimension, we measured in the reference image a few elements with known dimensions on the surface to monitor. According to the computation, the averaged pixel dimension is equal to 0.064 mm. We carried out the procedure considering the same time intervals adopted in the comparison between the fixed and the moving cameras on side A. The comparisons between the LVDT measurements and the crack aperture computed using *CMfM* are shown in Fig. 19.

Also, in this case, the results show a good agreement with the reference: the accuracy of the moving camera in estimating the crack width is of the order of a few hundredths of a millimetre and it is always below the pixel dimension. It is also worth noting that the LVDT returns the measurement only along a specific direction but it covers an extended portion of the image. The exact position of the LVDT measurement is, indeed, difficult to retrieve. Therefore, the comparison can be partially affected by small misalignments between the device and the camera measurement points.
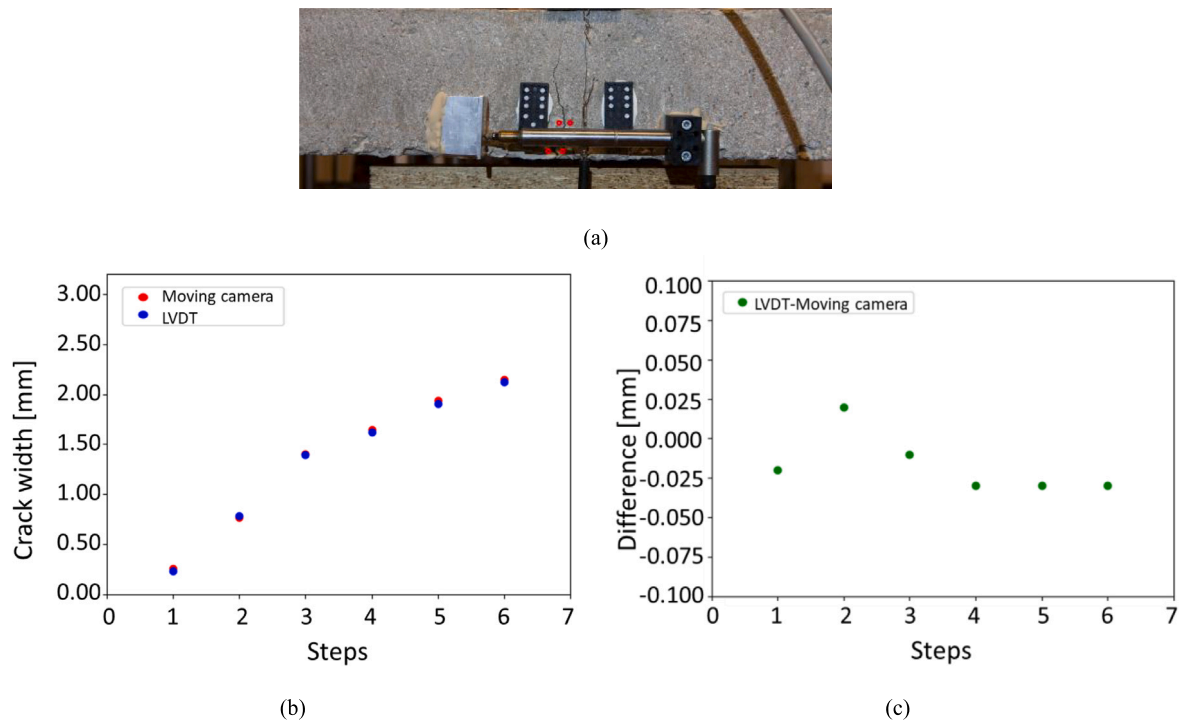
(a)

(b)

(c)

Fig. 19. Crack width comparison between *CMfM* and the LVDT.

4.2. Experimental test 2

The aim of the second case study was to measure the crack propagation in a cracked concrete beam using images acquired with a non-fixed camera at a larger distance from the beam. The setup consisted of an $800 \times 150 \times 150$ mm (length × width × height) cracked concrete beam subjected to three-point bending (Fig. 20).
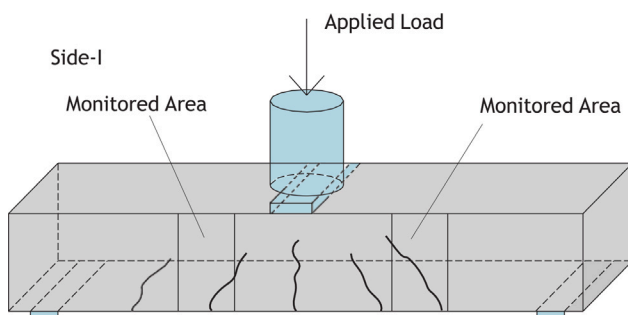

Fig. 20. Laboratory setup for the three-point bending test.

In this test, we employed a fixed Canon EOS 5D Mark 2 camera and a moving iPhone SE - 2022 (12 Megapixels). For each step, we maintained a constant loading and we captured images with the Canon camera at a distance of around 60 cm and with the iPhone SE from different camera poses at a distance of about 35 cm. To show the potential of *CMfM*, we processed the images with *CMfM* and the standard 2D DIC implemented in *Py2DIC*. For the sake of brevity, we show here only the results of one step in which the propagation of a new crack is evident. We considered three different poses of the iPhone SE and the corresponding images captured with the fixed camera. The results are presented in Fig. 21 and Table 2.

Again, the results highlight how the crack width computed using the moving camera and *CMfM* well follows the reference trend of the fixed camera and the DIC technique. Indeed, all the statistic values are below the pixel level (Table 2) which is equal to 0.9 mm in the reference image of the iPhone SE.

Table 2
Comparison between *CMfM* and DIC in one selected step considering three different image pairs.

Image pair	Mean [px]	Median [px]	Std Dev [px]	NMAD [px]
1	−0.35	−0.45	0.63	0.66
2	−0.66	−0.60	0.42	0.24
3	0.35	0.39	0.72	0.81

5. Conclusions and prospects

This paper proposed a novel methodology, named *Crack Monitoring from Motion* (*CMfM*), for the automatic detection of cracks and the monitoring of their in-plane evolution using cameras with non-fixed positions over time. Our main goal was to develop and test an innovative procedure able to overcome the limitations of standard sensors and well-established image-based techniques (e.g. DIC). Indeed, the proposed methodology does not require a fixed camera for image collection as well as targets or un-deformed regions inside the images. The unique additional required information is the presence of a reference scale (e.g. a ruler or an object with at least one known dimension) in the crack plane during the first epoch of measurement (t_0); the reference scale enables, indeed, the length conversion between pixel and metric units. Also, it is worth noticing that the accuracy of the results can be ensured by following best practices during data acquisition and processing:

- a condition of parallelism between the first image and the planar surface to monitor since this plane image implicitly defines the plane where the crack is detected and monitored over time;
- correction of geometric distortions using camera calibration models if needed;
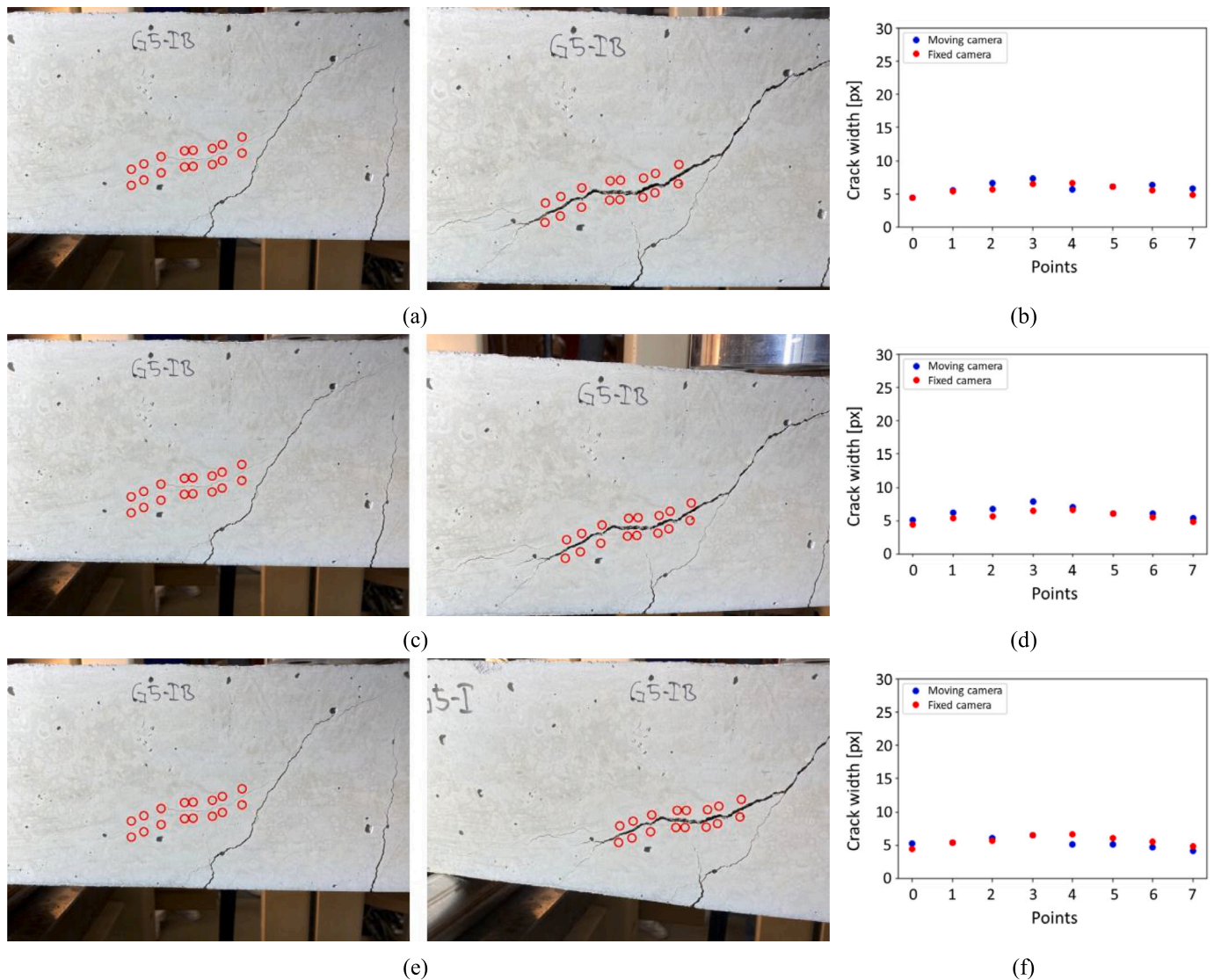
Fig. 21. Crack width comparison between *CMfM* and DIC - pair 1 (a, b), 2 (c, d), and 3 (e, f).

- use of cameras with a better resolution to achieve more accurate and detailed detection and measurements of cracks.

The potentialities of the *CMfM* methodology were evaluated by processing images acquired in two different laboratory tests and by comparing the results with those obtained employing the standard 2D DIC technique, i.e. analysing the images collected by fixed cameras, and an LVDT sensor. The results pointed out an accuracy of *CMfM* at the level of the pixel size compared to standard DIC and of a few hundredths of a millimetre compared to the LVDT reference measurements. It is worth mentioning that the images analysed in the experimental tests were captured using a standard smartphone camera, which makes the approach also suitable for low-cost effective inspections. This research has, therefore, the potential to contribute to the improvement of infrastructure monitoring efficiency and objectivity.

In the future, we plan to further test the implemented methodology in detecting and measuring crack propagation using images collected outside the controlled laboratory conditions. In particular, we intend to apply the methodology to multiple cracks visible in images collected using mobile mapping systems and also combine the methodology with Light Detection And Ranging (LiDAR) data to easily include the scale of the images.

Declaration of competing interest

The authors declare that they have no known competing financial interests or personal relationships that could have appeared to influence the work reported in this paper.

Data availability

Data are available on Mendeley Data [83,84]. Code will be available at https://github.com/Geod-Geom/CMfM.

Funding

Appendix. Experiments with synthetic data

Further validation of the proposed methodology involved the use of synthetic data to simulate different cracks and camera poses for assessing *CMfM* under ideal conditions. We generated regular planar points

representing a surface subjected to cracking and we projected them to image planes corresponding to different camera poses. According to a simplified scheme, we generated the first image parallel to the XY plane with a camera centre O_0 at a distance d from the planar surface (Fig. 22).
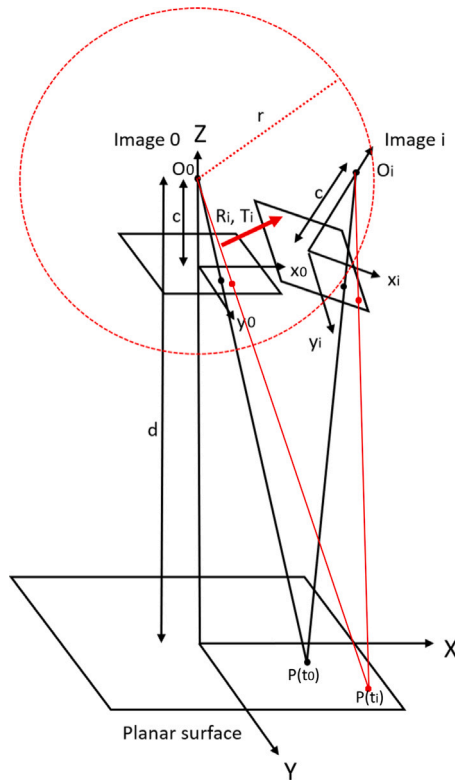

Fig. 22. Geometry of the simulations.

This means that the rotation matrix R_0 of the first image is equal to the identity matrix and the translation vector is $T_0 = (0, 0, d)$. Then, to simulate the O_i ($i = 1, \ldots, n$) camera centres of the n images, we generated random positions inside a sphere centred in O_0 with radius r.

To measure a deformation process, we simulated a crack with random orientation in the XY plane and we added the corresponding displacement patterns to the original points of the planar surface. To generate the crack, we randomly selected two points on the edges of the planar surface and we joined them to define the crack path. Then, we rotated the points on one side of the crack considering one of the two points on the edges as the rotation centre.

We retrieved the translation vectors $T_i = (Xo_i, Yo_i, Zo_i)$ and rotation matrices $R_i(\varphi_i, \lambda_i, k_i)$ of each ith camera configuration using the camera centres. We calculated the translations as the difference of the camera positions in the X, Y and Z directions and we obtained the rotation angles $(\varphi_i, \lambda_i, k_i)$ from the directional cosines of the straight line joining each O_i camera centre to a random point defined in the XY surface. Once the crack and the camera poses were defined, we projected all the points of the planar surface to each of the n image planes according to the following equation (Eq. (2)):

$$x_i = K \left| R_i | T_i \right| X_i \tag{2}$$

where:

- x_i is the vector containing the 2D point homogeneous coordinates of the ith image;
- K is the calibration matrix of the camera;
- R_i is the rotation matrix of the ith image;

- T_i is the translation vector of the ith image;
- X_i is the vector containing the 3D point coordinates of the grid points on the planar surface $(X, Y, 0)$ corresponding to each simulated crack at time t_i.

For the first reference image $I(t_0)$, we projected the points of the planar surface to the image plane without considering any deformation pattern. For all the other i images ($I(t_i)$ with $i = 1, \ldots, n$), we projected the points from the planar surface to each image after adding the displacement patterns due to cracking. We performed different simulations to investigate the robustness of the proposed model, also considering Gaussian errors to simulate the matching error in detecting the homologous points.

Simulations without Gaussian errors

We simulated cracks with random orientations on a planar surface considering different deformations. Then, we applied *CMfM* to estimate the crack propagation in the synthetic image planes. In this case, we generated the grids of points in the reference and in the deformed images directly during the simulation. For this reason, we did not adopt the SIFT algorithm to detect corresponding points on the image planes and we estimated the homography using all the generated points. After homography estimation, we projected the points of the ith image planes to the first one using the inverse of the estimated homography matrix. Then, we calculated the differences between the positions of the back-projected points (t_i) and their initial positions (t_0) in the first image, separately in the X and Y directions. We computed the crack aperture as the difference of the point position selected on the left and right sides of the crack.

During the simulation, we generated 100 cracks with different orientations. For each crack, we considered three steps of aperture (step 1, step 2, step 3) with increasing rotation angles $(1°, 2°, 3°)$ and three different camera poses to simulate real acquisitions during the crack propagation. For each simulation, we computed the signed differences between the generated and estimated crack aperture to define the error of the methodology. In terms of geometry, we defined the simulation parameters using real conditions of laboratory tests (camera focal length $c = 55$ mm, reference image distance from crack plane $d = 450$ mm, crack plane extension 201 mm × 201 mm). We used increasing radius r of the sphere centred in O_0 ($r = 10$ mm, $r = 20$ mm, $r = 30$ mm). We calculated the standard statistics (mean, median, standard deviation and NMAD) of the cumulative errors for all the cracks and geometries of the simulation globally and separately for each step. For the sake of brevity, we present in Table 3 only the results related to the most challenging configuration (radius $r = 30$ mm).

Table 3
Statistics of the errors obtained with 100 randomly simulated cracks and radius $r = 30$ mm.

	Mean [mm]	Median [mm]	Std Dev [mm]	NMAD [mm]
Overall	2.9e−10	4.1e−10	8.8e−09	6.5e−09
Step 1	3.4e−11	1.7e−10	4.6e−09	4.2e−09
Step 2	1.9e−10	2.5e−10	8.3e−09	7.5e−09
Step 3	−5.5e−11	3.1e−10	1.2e−08	1.1e−08

The quite similar mean and median values, one order of magnitude lower than similar standard deviation and NMAD values highlight the absence of biases and the overall implemented procedure accuracy at 10^{-9} millimetre level.

Finally, we computed the cumulative errors along the crack length for a detailed analysis of the results. We normalized each crack length of the simulation in the range $0 - 1$ and we computed the cumulative errors corresponding to six sections along the normalized crack lengths. We aggregated the errors of all the generated cracks by computing the

medians and 95% confidence intervals for each section. We performed the computation separately for each step of deformation. Fig. 23 shows the results related to step 3 (rotation of 3°). Again, the low medians and 95% confidence intervals indicate the robustness of the approach.
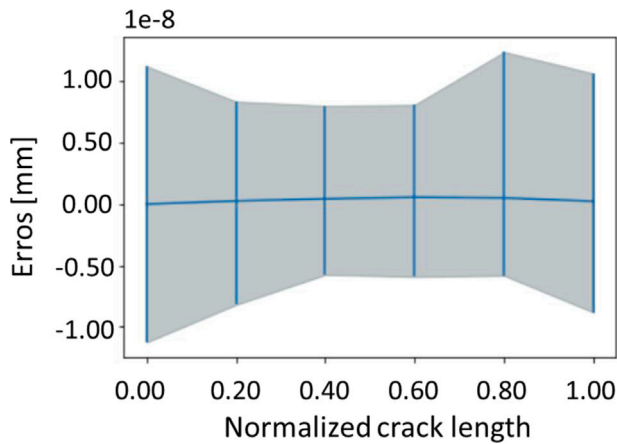

Fig. 23. Results of the simulations obtained with 100 randomly simulated cracks, 3° of crack aperture and radius $r = 30$ mm.

Simulations with Gaussian errors

We performed a second simulation to investigate the impact of errors that can arise during the matching procedure. We generated random errors using the Gaussian distributions and we added them to the horizontal and vertical displacement fields, separately. We adopted Gaussian distributions with mean and standard deviation equal to μ_{disp} = 0 mm and σ_{displ} = 0.05 mm, respectively. We set the value of the standard deviation equal to σ_{displ} = 0.05 mm to consider an error due to the matching procedure that is twice the pixel dimension of a real laboratory test. Fig. 24 shows an example of crack displacement fields with Gaussian errors.
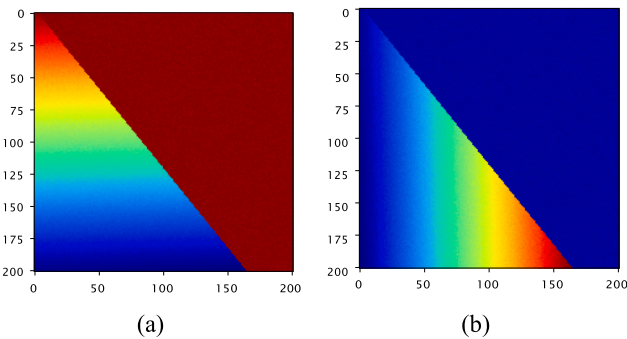

Fig. 24. Horizontal (a) and vertical (b) displacement fields [mm] with random Gaussian errors.

We computed the errors of the simulations as described in the previous simulation. We present in Table 4 only the results related to radius $r = 30$ mm.

Table 4
Statistics of the errors obtained with 100 randomly simulated cracks, gaussian errors and radius $r = 30$ mm.

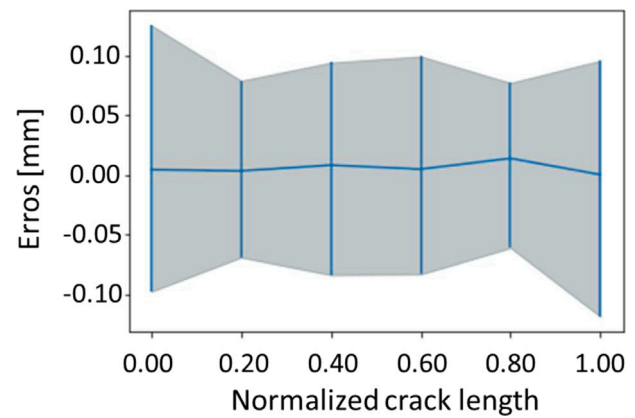|	Mean [mm]	Median [mm]	Std Dev [mm]	NMAD [mm]
Overall	0.001	0.000	0.071	0.071
Step 1	0.001	−0.000	0.070	0.071
Step 2	0.000	0.000	0.071	0.071
Step 3	0.001	0.001	0.071	0.071

Fig. 25. Results of the simulations obtained with 100 randomly simulated cracks and random Gaussian errors, 3° of crack aperture and radius $r = 30$ mm.

Again, the quite similar mean and median values, one/two orders of magnitudes lower than quite similar standard deviation and NMAD values highlight the absence of biases and the overall accuracy at the level of $\sqrt{2}\sigma_{displ}$, as expected in case of independent added errors. Finally, Fig. 25 shows the medians and 95% confidence intervals of the errors computed over six sections along the normalized crack length (step 3).

References

[1] James M.W. Brownjohn, Structural health monitoring of civil infrastructure, Phil. Trans. R. Soc. A 365 (1851) (2007) 589–622, http://dx.doi.org/10.1098/rsta.2006.1925.

[2] Nhat-Duc Hoang, Detection of surface crack in building structures using image processing technique with an improved Otsu method for image thresholding, Adv. Civ. Eng. (2018) http://dx.doi.org/10.1155/2018/3924120.

[3] Christian Koch, Kristina Georgieva, Varun Kasireddy, Burcu Akinci, Paul Fieguth, A review on computer vision based defect detection and condition assessment of concrete and asphalt civil infrastructure, Adv. Eng. Inform. 29 (2) (2015) 196–210, http://dx.doi.org/10.1016/j.aei.2015.01.008, Infrastructure Computer Vision.

[4] Dhirendranath Thatoi, Punyaslok Guru, Prabir Kumar Jena, Sasanka Choudhury, Harish Chandra Das, Comparison of CFBP, FFBP, and RBF networks in the field of crack detection, Model. Simul. Eng. 2014 (2014) http://dx.doi.org/10.1155/2014/292175.

[5] Hamidreza Salehian, Joaquim A.O. Barros, Mahsa Taheri, Evaluation of the influence of post-cracking response of steel fibre reinforced concrete (SFRC) on load carrying capacity of SFRC panels, Constr. Build. Mater. 73 (2014) 289–304, http://dx.doi.org/10.1016/j.conbuildmat.2014.09.043.

[6] Javad Baqersad, Peyman Poozesh, Christopher Niezrecki, Peter Avitabile, Photogrammetry and optical methods in structural dynamics – A review, Mech. Syst. Signal Process. 86 (2017) 17–34, http://dx.doi.org/10.1016/j.ymssp.2016.02.011, Full-field, non-contact vibration measurement methods: comparisons and applications.

[7] Giorgio Busca, Alfredo Cigada, Paolo Mazzoleni, Emanuele Zappa, Vibration monitoring of multiple bridge points by means of a unique vision-based measuring system, Exp. Mech. 54 (2014) 255–271, http://dx.doi.org/10.1007/s11340-013-9784-8.

[8] Yoshio Fukuda, Maria Q. Feng, Masanobu Shinozuka, Cost-effective vision-based system for monitoring dynamic response of civil engineering structures, Struct. Control Health Monit. 17 (8) (2010) 918–936, http://dx.doi.org/10.1002/stc.360.

[9] Piotr Kohut, Krzysztof Holak, Tadeusz Uhl, Łukasz Ortyl, Tomasz Owerko, Przemysław Kuras, Rafał Kocierz, Monitoring of a civil structure's state based on noncontact measurements, Struct. Health Monit. 12 (5–6) (2013) 411–429, http://dx.doi.org/10.1177/1475921713487397.

[10] Bing Pan, Kemao Qian, Huimin Xie, Anand Asundi, Topical Review: Two-dimensional digital image correlation for in-plane displacement and strain measurement: a review, Meas. Sci. Technol. 20 (2009) http://dx.doi.org/10.1088/0957-0233/20/6/062001.

[11] Valeria Belloni, Andreas Sjölander, Roberta Ravanelli, Mattia Crespi, Andrea Nascetti, Tack project: Tunnel and bridge automatic crack monitoring using deep learning and photogrammetry, Int. Arch. Photogramm. Remote Sens. Spatial Inf. Sci. XLIII-B4-2020 (2020) 741–745, http://dx.doi.org/10.5194/isprs-archives-XLIII-B4-2020-741-2020.

[12] Andreas Sjölander, Valeria Belloni, Anders Ansell, Erik Nordström, Towards automated inspections of tunnels: A review of optical inspections and autonomous assessment of concrete tunnel linings, Sensors 23 (6) (2023) http://dx.doi.org/10.3390/s23063189.

[13] Luigi Barazzetti, Marco Scaioni, Crack measurement: Development, testing and applications of an automatic image-based algorithm, ISPRS J. Photogramm. Remote Sens. 64 (3) (2009) 285–296, http://dx.doi.org/10.1016/j.isprsjprs.2009.02.004, Theme Issue: Image Analysis and Image Engineering in Close Range Photogrammetry.

[14] Valeria Belloni, Roberta Ravanelli, Andrea Nascetti, Martina Di Rita, Domitilla Mattei, Mattia Crespi, py2DIC: A new free and open source software for displacement and strain measurements in the field of experimental mechanics, Sensors 19 (18) (2019) 3832, http://dx.doi.org/10.3390/s19183832.

[15] Richard Malm, Full-scale test of an unreinforced concrete dome plug for the spent nuclear fuel repository, Nord. Concr. Res. 58 (2018) 55–75, http://dx.doi.org/10.2478/ncr-2018-0004.

[16] D. Benoit Jones, A 20 year history of stress and strain in a shotcrete primary, in: 8th International Symposium on Sprayed Concrete, 2018.

[17] Christopher K.Y. Leung, Fiber optic sensors in concrete: the future? NDT & E Int. 34 (2) (2001) 85–94, http://dx.doi.org/10.1016/S0963-8695(00)00033-5.

[18] Luigi Barazzetti, Marco Scaioni, Development and implementation of image-based algorithms for measurement of deformations in material testing, Sensors 10 (2010) 7469–7495, http://dx.doi.org/10.3390/s100807469.

[19] Kort Bremer, Frank Weigand, Yulong Zheng, Lourdes Shanika Alwis, Reinhard Helbig, Bernhard Roth, Structural health monitoring using textile reinforcement structures with integrated optical fiber sensors, Sensors 17 (2017) 345, http://dx.doi.org/10.3390/s17020345.

[20] Nobuyuki Otsu, A threshold selection method from gray-level histograms, IEEE Trans. Syst. Man Cybern. 9 (1) (1979) 62–66, http://dx.doi.org/10.1109/TSMC.1979.4310076.

[21] Hyunjun Kim, Eunjong Ahn, Soojin Cho, Myoungsu Shin, Sung-Han Sim, Comparative analysis of image binarization methods for crack identification in concrete structures, Cem. Concr. Res. 99 (2017) http://dx.doi.org/10.1016/J.CEMCONRES.2017.04.018.

[22] Hong-Gyoo Sohn, Yun-Mook Lim, Kong-Hyun Yun, Gi-Hong Kim, Monitoring crack changes in concrete structures, Comput.-Aided Civ. Infrastruct. Eng. 20 (1) (2005) 52–61, http://dx.doi.org/10.1111/j.1467-8667.2005.00376.x.

[23] Akira Ito, Yoshimitsu Aoki, Shuji Hashimoto, Accurate extraction and measurement of fine cracks from concrete block surface image, in: IEEE 2002 28th Annual Conference of the Industrial Electronics Society. IECON 02, 3, 2002, pp. 2202–2207, http://dx.doi.org/10.1109/IECON.2002.1185314.

[24] Bang Yeon Lee, Yun Yong Kim, Seong-Tae Yi, Jin-Keun Kim, Automated image processing technique for detecting and analysing concrete surface cracks, Struct. Infrastruct. Eng. 9 (6) (2013) 567–577, http://dx.doi.org/10.1080/15732479.2011.593891.

[25] Sattar Dorafshan, Marc Maguire, Xiaojun Qi, Automatic Surface Crack Detection in Concrete Structures Using OTSU Thresholding and Morphological Operations, Technical report, 2016, http://dx.doi.org/10.13140/RG.2.2.34024.47363.

[26] Seung-Nam Yu, Jae-Ho Jang, Chang-Soo Han, Auto inspection system using a mobile robot for detecting concrete cracks in a tunnel, Autom. Constr. 16 (3) (2007) 255–261, http://dx.doi.org/10.1016/j.autcon.2006.05.003.

[27] Wenyu Zhang, Zhenjiang Zhang, Dapeng Qi, Yun Liu, Automatic crack detection and classification method for subway tunnel safety monitoring, Sensors 14 (10) (2014) 19307–19328, http://dx.doi.org/10.3390/s141019307.

[28] Tomoyuki Yamaguchi, Shuji Hashimoto, Automated crack detection for concrete surface image using percolation model and edge information, in: IECON 2006 - 32nd Annual Conference on IEEE Industrial Electronics, 2006, pp. 3355–3360, http://dx.doi.org/10.1109/IECON.2006.348070.

[29] Tomoyuki Yamaguchi, Shuji Hashimoto, Practical image measurement of crack width for real concrete structure, Electron. Commun. Japan 92 (10) (2009) 1–12, http://dx.doi.org/10.1002/ecj.10151.

[30] Paul Dare, Harry Hanley, Clive Fraser, Björn Riedel, Wolfgang Niemeier, An operational application of automatic feature extraction: The measurement of cracks in concrete structures, Photogramm. Rec. 17 (99) (2002) 453–464, http://dx.doi.org/10.1111/0031-868X.00198.

[31] Liang-Chien Chen, Yi-Chen Shao, Huang-Hsiang Jan, Chen-Wei Huang, Yong-Ming Tien, Measuring system for cracks in concrete using multitemporal images, J. Surv. Eng. 132 (2) (2006) 77–82, http://dx.doi.org/10.1061/(ASCE)0733-9453(2006)132:2(77).

[32] Daniel Dias-da Costa, Jónatas Valença, Eduardo N.B.S. Júlio, Laboratorial test monitoring applying photogrammetric post-processing procedures to surface displacements, Measurement 44 (3) (2011) 527–538, http://dx.doi.org/10.1016/j.measurement.2010.11.014.

[33] Jónatas Valença, Daniel Dias-da Costa, Eduardo N.B.S. Júlio, Helder Araújo, Hugo Costa, Automatic crack monitoring using photogrammetry and image processing, Measurement 46 (1) (2013) 433–441, http://dx.doi.org/10.1016/j.measurement.2012.07.019.

[34] Ruoxing Li, Yachao Yuan, Wei Zhang, Yali Yuan, Unified vision-based methodology for simultaneous concrete defect detection and geolocalization, Comput.-Aided Civ. Infrastruct. Eng. 33 (7) (2018) 527–544, http://dx.doi.org/10.1111/mice.12351.

[35] Young-Jin Cha, Wooram Choi, Oral Buyukozturk, Deep learning-based crack damage detection using convolutional neural networks, Comput.-Aided Civ. Infrastruct. Eng. 32 (2017) 361–378, http://dx.doi.org/10.1111/mice.12263.

[36] Kasthurirangan Gopalakrishnan, Siddhartha K. Khaitan, Alok Choudhary, Ankit Agrawal, Deep convolutional neural networks with transfer learning for computer vision-based data-driven pavement distress detection, Constr. Build. Mater. 157 (2017) 322–330, https://doi.org/10.1016/j.conbuildmat.2017.09.110.

[37] Qin Zou, Zheng Zhang, Qingquan Li, Xianbiao Qi, Qian Wang, Song Wang, DeepCrack: Learning hierarchical convolutional features for crack detection, IEEE Trans. Image Process. 28 (3) (2019) 1498–1512, http://dx.doi.org/10.1109/TIP.2018.2878966.

[38] Zhenqing Liu, Yiwen Cao, Yize Wang, Wei Wang, Computer vision-based concrete crack detection using U-net fully convolutional networks, Autom. Constr. 104 (2019) 129–139, http://dx.doi.org/10.1016/j.autcon.2019.04.005.

[39] Yupeng Ren, Jisheng Huang, Zhiyou Hong, Wei Lu, Jun Yin, Lejun Zou, Xiaohua Shen, Image-based concrete crack detection in tunnels using deep fully convolutional networks, Constr. Build. Mater. 234 (2020) 117367, http://dx.doi.org/10.1016/j.conbuildmat.2019.117367.

[40] Olaf Ronneberger, Philipp Fischer, Thomas Brox, U-Net: Convolutional networks for biomedical image segmentation, in: Nassir Navab, Joachim Hornegger, William M. Wells, Alejandro F. Frangi (Eds.), Medical Image Computing and Computer-Assisted Intervention, MICCAI 2015, Springer International Publishing, Cham, 2015, pp. 234–241, http://dx.doi.org/10.1007/978-3-319-24574-4_28.

[41] Tsuchin Chu, William Ranson, Michael Sutton, Applications of digital-image-correlation techniques to experimental mechanics, Exp. Mech. 25 (1985) 232–244, http://dx.doi.org/10.1007/BF02325092.

[42] Justin Blaber, Benjamin Adair, Antonia Antoniou, Ncorr: Open-source 2D digital image correlation matlab software, Exp. Mech. 55 (2015) http://dx.doi.org/10.1007/s11340-015-0009-1.

[43] Tahreer M. Fayyad, Janet M. Lees, Application of digital image correlation to reinforced concrete fracture, Proc. Mater. Sci. 3 (2014) 1585–1590, http://dx.doi.org/10.1016/j.mspro.2014.06.256, 20th European Conference on Fracture.

[44] Satoru Yoneyama, Hisao Kikuta, Akikazu Kitagawa, Koji Kitamura, Lens distortion correction for digital image correlation by measuring rigid body displacement, Opt. Eng. 45 (2006) http://dx.doi.org/10.1117/1.2168411.

[45] Satoru Yoneyama, Akikazu Kitagawa, Koji Kitamura, Hisao Kikuta, In-plane displacement measurement using digital image correlation with lens distortion correction, JSME Int. J. Ser. A 49 (3) (2006) 458–467, http://dx.doi.org/10.1299/jsmea.49.458.

[46] Dongming Feng, Maria Q. Feng, Ekin Ozer, Yoshio Fukuda, A vision-based sensor for noncontact structural displacement measurement, Sensors 15 (7) (2015) 16557–16575, http://dx.doi.org/10.3390/s150716557.

[47] Ala Hijazi, Alexandra Friedl, Christian Kähler, Influence of camera's optical axis non-perpendicularity on measurement accuracy of two-dimensional digital image correlation, Jordan J. Mech. Ind. Eng. 5 (2011) 373–382.

[48] Bing Pan, Liping Yu, Dafang Wu, Liqun Tang, Systematic errors in two-dimensional digital image correlation due to lens distortion, Opt. Lasers Eng. 51 (2) (2013) 140–147, http://dx.doi.org/10.1016/j.optlaseng.2012.08.012.

[49] Michael A. Sutton, Junhui Yan, Vikrant Tiwari, Hubert W. Schreier, Jean José Orteu, The effect of out-of-plane motion on 2D and 3D digital image correlation measurements, Opt. Lasers Eng. 46 (10) (2008) 746–757, http://dx.doi.org/10.1016/j.optlaseng.2008.05.005.

[50] François Hild, Stephane Roux, Comparison of local and global approaches to digital image correlation, Exp. Mech. 52 (2012) http://dx.doi.org/10.1007/s11340-012-9603-7.

[51] Bo Wang, Bing Pan, Subset-based local vs. finite element-based global digital image correlation: A comparison study, Theor. Appl. Mech. Lett. 6 (5) (2016) 200–208, http://dx.doi.org/10.1016/j.taml.2016.08.003.

[52] Syed Alam, Ahmed Loukili, Frédéric Grondin, Monitoring size effect on crack opening in concrete by digital image correlation, Eur. J. Environ. Civ. Eng. 16 (2012) 1–19, http://dx.doi.org/10.1080/19648189.2012.672211.

[53] Mostefa Hamrat, Bensaid Boulekbache, Mohamed Chemrouk, Sofiane Amziane, Flexural cracking behavior of normal strength, high strength and high strength fiber concrete beams, using digital image correlation technique, Constr. Build. Mater. 106 (2016) 678–692, http://dx.doi.org/10.1016/j.conbuildmat.2015.12.166.

[54] Michel Küntz, Marc Jolin, J. Bastien, Fabien Perez, François Hild, Digital image correlation analysis of crack behavior in a reinforced concrete beam during a load test, Can. J. Civil Eng. 33 (2011) 1418–1425, http://dx.doi.org/10.1139/l06-106.

[55] Florent Mathieu, François Hild, Stéphane Roux, Identification of a crack propagation law by digital image correlation, Int. J. Fatigue 36 (1) (2012) 146–154, http://dx.doi.org/10.1016/j.ijfatigue.2011.08.004.

[56] Julien Réthoré, François Hild, Stéphane Roux, Extended digital image correlation with crack shape optimization, Internat. J. Numer. Methods Engrg. 73 (2) (2008) 248–272, http://dx.doi.org/10.1002/nme.2070.

[57] Bruno Santos, Jónatas Valença, Eduardo Júlio, Monitoring cracks on concrete surfaces using multi-temporal images, in: 40th IABSE Symposium, 2018, http://dx.doi.org/10.2749/nantes.2018.s24-95.

[58] Nicola Gehri, Jaime Mata-Falcón, Walter Kaufmann, Automated crack detection and measurement based on digital image correlation, Constr. Build. Mater. 256 (2020) 119383, http://dx.doi.org/10.1016/j.conbuildmat.2020.119383.

[59] Christian Overgaard Christensen, Jacob Wittrup Schmidt, Philip Skov Halding, Medha Kapoor, Per Goltermann, Digital image correlation for evaluation of cracks in reinforced concrete bridge slabs, Infrastructures 6 (7) (2021) http://dx.doi.org/10.3390/infrastructures6070099.

[60] Liu Rui, Emanuele Zappa, Andrea Collina, Vision-based measurement of crack generation and evolution during static testing of concrete sleepers, Eng. Fract. Mech. 224 (2020) 106715, http://dx.doi.org/10.1016/j.engfracmech.2019.106715.

[61] Egil Fagerholt, Erling Østby, Tore Børvik, Odd Sture Hopperstad, Investigation of fracture in small-scale SENT tests of a welded X80 pipeline steel using digital image correlation with node splitting, Eng. Fract. Mech. 96 (2012) 276–293, http://dx.doi.org/10.1016/j.engfracmech.2012.08.007.

[62] Jeffrey Helm, Digital image correlation for specimens with multiple growing cracks, Exp. Mech. 48 (2008) 753–762, http://dx.doi.org/10.1007/s11340-007-9120-2.

[63] Chuan-Zhi Dong, Ozan Celik, Necati Catbas, Eugene OBrien, Su Taylor, Structural displacement monitoring using deep learning-based full field optical flow methods, Struct. Infrastruct. Eng. (2019) 1–21, http://dx.doi.org/10.1080/15732479.2019.1650078.

[64] Satoru Yoneyama, Hiroki Ueda, Bridge deflection measurement using digital image correlation with camera movement correction, Mater. Trans. 53 (2012) 285–290, http://dx.doi.org/10.2320/matertrans.I-M2011843.

[65] Satoshi Nishiyama, Nao Minakata, Teruyuki Kikuchi, Takao Yano, Improved digital photogrammetry technique for crack monitoring, Adv. Eng. Inform. 29 (4) (2015) 851–858, http://dx.doi.org/10.1016/j.aei.2015.05.005.

[66] Karen Simonyan, Andrew Zisserman, Very deep convolutional networks for large-scale image recognition, Int. Conf. Learn. Represent. (2015) http://dx.doi.org/10.48550/arXiv.1409.1556.

[67] Olga Russakovsky, Jia Deng, Hao Su, Jonathan Krause, Sanjeev Satheesh, Sean Ma, Zhiheng Huang, Andrej Karpathy, Aditya Khosla, Michael Bernstein, Alexander C. Berg, Li Fei-Fei, ImageNet large scale visual recognition challenge, Int. J. Comput. Vis. (IJCV) 115 (3) (2015) 211–252, http://dx.doi.org/10.1007/s11263-015-0816-y.

[68] Khanh Ha, Crack segmentation, 2019, https://github.com/khanhha/crack_segmentation. (Accessed December 2022).

[69] Lei Zhang, Fan Yang, Yimin Daniel Zhang, Ying Julie Zhu, Road crack detection using deep convolutional neural network, in: 2016 IEEE International Conference on Image Processing, ICIP, 2016, pp. 3708–3712, http://dx.doi.org/10.1109/ICIP.2016.7533052.

[70] Fan Yang, Lei Zhang, Sijia Yu, Danil Prokhorov, Xue Mei, Haibin Ling, Feature pyramid and hierarchical boosting network for pavement crack detection, IEEE Trans. Intell. Transp. Syst. (2019) 1–11, http://dx.doi.org/10.1109/TITS.2019.2910595.

[71] Markus Eisenbach, Ronny Stricker, Daniel Seichter, Karl Amende, Klaus Debes, Maximilian Sesselmann, Dirk Ebersbach, Ulrike Stoeckert, Horst-Michael Gross, How to get pavement distress detection ready for deep learning? A systematic approach, in: 2017 International Joint Conference on Neural Networks, IJCNN, 2017, pp. 2039–2047, http://dx.doi.org/10.1109/IJCNN.2017.7966101.

[72] Yong Shi, Limeng Cui, Zhiquan Qi, Fan Meng, Zhensong Chen, Automatic road crack detection using random structured forests, IEEE Trans. Intell. Transp. Syst. 17 (12) (2016) 3434–3445, http://dx.doi.org/10.1109/TITS.2016.2552248.

[73] Rabih Amhaz, Sylvie Chambon, Jérôme Idier, Vincent Baltazart, Automatic crack detection on two-dimensional pavement images: An algorithm based on minimal path selection, IEEE Trans. Intell. Transp. Syst. 17 (10) (2016) 2718–2729, http://dx.doi.org/10.1109/TITS.2015.2477675.

[74] Qin Zou, Yu Cao, Qingquan Li, Qingzhou Mao, Song Wang, CrackTree: Automatic crack detection from pavement images, Pattern Recognit. Lett. 33 (3) (2012) 227–238, http://dx.doi.org/10.1016/j.patrec.2011.11.004.

[75] Andreas Sjölander, Valeria Belloni, Roberta Ravanelli, Kepan Gao, Andrea Nascetti, TACK – an autonomous inspection system for tunnels, in: ITA-AITES World Tunnel Congress, WTC2022 and 47th General Assembly, 2022.

[76] Albumentations library, 2022, https://pypi.org/project/albumentations/. (Accessed December 2022).

[77] Diederik P. Kingma, Jimmy Ba, Adam: A method for stochastic optimization, 2014, http://dx.doi.org/10.48550/arXiv.1412.6980, arXiv preprint arXiv:1412.6980.

[78] David Lowe, Distinctive image features from scale-invariant keypoints, Int. J. Comput. Vis. 60 (2004) 91, http://dx.doi.org/10.1023/B:VISI.0000029664.99615.94.

[79] Martin A. Fischler, Robert C. Bolles, Random Sample Consensus: A paradigm for model fitting with applications to image analysis and automated cartography, Commun. ACM 24 (6) (1981) 381–395, http://dx.doi.org/10.1145/358669.358692.

[80] Peter J. Rousseeuw, Least median of squares regression, J. Amer. Statist. Assoc. 79 (388) (1984) 871–880, http://dx.doi.org/10.1080/01621459.1984.10477105.

[81] Kenneth Levenberg, A method for the solution of certain non – linear problems in least squares, Quart. Appl. Math. 2 (1944) 164–168.

[82] Donald W. Marquardt, An algorithm for least-squares estimation of nonlinear parameters, J. Soc. Ind. Appl. Math. 11 (2) (1963) 431–441, http://dx.doi.org/10.1137/0111030.

[83] Andreas Sjölander, Valeria Belloni, Andrea Nascetti, Dataset to track concrete cracking using DIC with fixed and moving camera, Mendeley Data, V1, 2022. http://dx.doi.org/10.17632/dns97tfdjn.1.

[84] Andreas Sjölander, Valeria Belloni, Viktor Peterson, Jonatan Ledin, Monitoring of structural performance of cracked reinforced concrete using DIC and CMfM, Mendeley Data, V2, 2023. http://dx.doi.org/10.17632/z3yc9z84tk.2.

[85] Roberta Ravanelli, Andrea Nascetti, Martina Di Rita, Valeria Belloni, Domitilla Mattei, Nicola Nisticó, Mattia Crespi, A new digital image correlation software for displacements field measurement in structural applications, Int. Arch. Photogramm. Remote Sens. Spatial Inf. Sci. XLII-4/W2 (2017) 139–145, http://dx.doi.org/10.5194/isprs-archives-XLII-4-W2-139-2017.

[86] Valeria Belloni, Roberta Ravanelli, Andrea Nascetti, Martina Di Rita, Domitilla Mattei, Mattia Crespi, Digital image correlation from commercial to FOS software: a mature technique for full-field displacement measurements, Int. Arch. Photogramm. Remote Sens. Spatial Inf. Sci. 422 (2018) 91–95, http://dx.doi.org/10.5194/isprs-archives-XLII-2-91-2018.